



# Evidence for a sulfur-undersaturated lunar interior from the solubility of sulfur in lunar melts and sulfide-silicate partitioning of siderophile elements

E.S. Steenstra<sup>a,b,\*</sup>, A.X. Seegers<sup>a</sup>, J. Eising<sup>a</sup>, B.G.J. Tomassen<sup>a</sup>, F.P.F. Webers<sup>a</sup>, J. Berndt<sup>c</sup>, S. Klemme<sup>c</sup>, S. Matveev<sup>d</sup>, W. van Westrenen<sup>a</sup>

<sup>a</sup> Faculty of Science, Vrije Universiteit, Amsterdam, The Netherlands

<sup>b</sup> The Geophysical Laboratory, Carnegie Institution of Science, Washington D.C., United States

<sup>c</sup> Institute of Mineralogy, University of Münster, Germany

<sup>d</sup> Faculty of Geosciences, Utrecht University, The Netherlands

Received 21 December 2017; accepted in revised form 5 April 2018; Available online 14 April 2018

## Abstract

Sulfur concentrations at sulfide saturation (SCSS) were determined for a range of low- to high-Ti lunar melt compositions (synthetic equivalents of Apollo 14 black and yellow glass, Apollo 15 green glass, Apollo 17 orange glass and a late-stage lunar magma ocean melt, containing between 0.2 and 25 wt.% TiO<sub>2</sub>) as a function of pressure (1–2.5 GPa) and temperature (1683–1883 K). For the same experiments, sulfide-silicate partition coefficients were derived for elements V, Cr, Mn, Co, Cu, Zn, Ga, Ge, As, Se, Mo, Sn, Sb, Te, W and Pb. The SCSS is a strong function of silicate melt composition, most notably FeO content. An increase in temperature increases the SCSS and an increase in pressure decreases the SCSS, both in agreement with previous work on terrestrial, lunar and martian compositions. Previously reported SCSS values for high-FeO melts were combined with the experimental data reported here to obtain a new predictive equation to calculate the SCSS for high-FeO lunar melt compositions. Calculated SCSS values, combined with previously estimated S contents of lunar low-Ti basalts and primitive pyroclastic glasses, suggest their source regions were not sulfide saturated. Even when correcting for the currently inferred maximum extent of S degassing during or after eruption, sample S abundances are still > 700 ppm lower than the calculated SCSS values for these compositions. To achieve sulfide saturation in the source regions of low-Ti basalts and lunar pyroclastic glasses, the extent of degassing of S in lunar magma would have to be orders of magnitude higher than currently thought, inconsistent with S isotopic and core-to-rim S diffusion profile data. The only lunar samples that could have experienced sulfide saturation are some of the more evolved A17 high-Ti basalts, if sulfides are Ni- and/or Cu rich.

Sulfide saturation in the source regions of lunar melts is also inconsistent with the sulfide-silicate partitioning systematics of Ni, Co and Cu. Segregation of significant quantities of (non)-stoichiometric sulfides during fractional crystallization would result in far larger depletions of Ni, Co and Cu than observed, whereas trends in their abundances are more likely explained by olivine fractionation. The sulfide exhaustion of the lunar magma source regions agrees with previously proposed low S abundances in the lunar core and mantle, and by extension with relatively minor degassing of S during the Moon-forming event. Our results support the hypothesis that refractory chalcophile and highly siderophile element systematics of low-Ti basalts and pyroclastic glasses reflect the geochemical characteristics of their source regions, instead of indicating the presence of residual sulfides in the lunar interior.

© 2018 Elsevier Ltd. All rights reserved.

**Keywords:** Moon; Volatiles; Siderophile; Chalcophile; Sulfides; SCSS

\* Corresponding author at: Faculty of Science, Vrije Universiteit, Amsterdam, The Netherlands.

E-mail address: [e.s.steenstra@vu.nl](mailto:e.s.steenstra@vu.nl) (E.S. Steenstra).

## 1. INTRODUCTION

Sulfur (S) is a volatile element and understanding its origin, abundance, and distribution in planetary interiors is important due to the effects of the sulfur cycle on properties of planetary crusts, atmospheres and, in the case of the Earth, the biosphere (Farquhar et al., 2000). Constraining S abundances in lunar reservoirs is important to constrain the early volatile budget of, and volatile fluxes in, the Earth-Moon system (e.g., Wing and Farquhar, 2015; Righter et al., 2017a,b; Steenstra et al., 2017a,b). One key aspect of the lunar sulfur cycle relates to the question whether the lunar interior was ever saturated in sulfide minerals. Sulfides are sinks for chalcophile elements that will preferentially partition into these phases (Kiseeva and Wood, 2013; Mungall and Brenan, 2014; Wood et al., 2014; Steenstra et al., 2017a). Many of the chalcophile elements are also (highly) volatile and their depletion in samples derived from the lunar interior may provide important constraints on models of the early evolution of the Earth-Moon system (Paniello et al., 2012; Wang and Becker, 2013; Steenstra et al., 2016; Wang et al., 2016; Kato and Moynier, 2017; Righter et al., 2017a,b). Quantifying chalcophile element depletions however requires knowledge about the presence or absence of sulfides in the lunar interior. The interpretations of the systematics of highly siderophile element (HSE's) abundances in lunar samples are also highly dependent on the assumption of sulfide undersaturation or saturation in the lunar mantle, given the fact that the HSE behave significantly less siderophile in the presence of FeS (Mungall and Brenan, 2014; Laurenz et al., 2016).

Several previous studies focused on determination of the SCSS of terrestrial compositions (Wendlandt, 1982; Mavrogenes and O'Neill, 1999; Liu et al., 2007; Jugo et al., 2005; Wykes et al., 2015; Fortin et al., 2015; Smythe et al., 2017). Lunar melts are distinctly different due to their higher TiO<sub>2</sub> and FeO contents, where low-Ti basalts contain < 6 wt.% TiO<sub>2</sub> and high-Ti basalts > 6 wt.% (Neal and Taylor, 1992). Some studies determined the SCSS values for high-FeO martian basalts, but these compositions have low TiO<sub>2</sub> contents (Righter et al., 2009; Ding et al., 2014). Only three studies experimentally determined the solubility of S for a limited range of high-Ti lunar melt compositions (Danckwerth et al., 1979; O'Neil and Mavrogenes, 2002; Ding et al., 2017).

Gibson et al. (1975, 1976) and Brett (1976) argued for sulfide saturation in the Apollo 17 source regions, based on SCSS data of terrestrial basalts. The latter studies did not explore the effects of pressure (*P*), temperature (*T*) or a wider range of (lunar) melt compositions. Danckwerth et al. (1979) studied the solubility of S in the A17 high-Ti basalt 74275 as a function of its FeO content and found that up to 3400 ppm S could be dissolved in this composition at a temperature of 1523 K and a pressure of 1 bar. Given the S contents measured in this basalt, they concluded that A17 high TiO<sub>2</sub> basalts were not sulfide saturated near their liquidus temperatures. O'Neil and Mavrogenes (2002) studied the overall effects of TiO<sub>2</sub> and reported a subtle increase of SCSS with increasing silicate melt TiO<sub>2</sub> content. The most recent study (Ding et al., 2017) experimentally determined the SCSS for an average Luna 16 mare basalt composition (TiO<sub>2</sub> ~5 wt.%) and the Apollo 11 B3 mare basalt (TiO<sub>2</sub> ~11 wt.%). Using a revised model for predicting the SCSS, Ding et al. (2017) found that the SCSS at the conditions of last equilibration of intermediate and high-Ti lunar basalts and glasses are higher than the measured S contents in these samples. This suggests that no sulfide retention occurred in the lunar mantle during these partial melting events.

Determination of the SCSS for low- and high-Ti melts over a wide *P-T* and compositional range is required to assess if the source regions of lunar magmas sampled during the Apollo missions were sulfide saturated. Here, we quantify the SCSS for a suite of low- to high-Ti lunar melt compositions (synthetic equivalents of Apollo 14 (A14) black and yellow glass, Apollo 15 (A15) green glass, Apollo 17 (A17) orange glass and a composition representative of late-stage lunar magma ocean (LMO) residual melt), together covering a range in TiO<sub>2</sub> content of 0.2–25 wt.%, as a function of *P-T* (Tables 1–4). The new SCSS dataset is combined with previously determined SCSS data for high-FeO silicate melts to obtain predictive SCSS model values specifically suitable for high-FeO lunar melts. This model is then used to calculate the SCSS values for the various lunar low- and high-Ti melts and resulting values are compared with the measured S contents in these samples to assess the likelihood of sulfide saturation in their source regions.

Sulfide saturation in the lunar mantle can also be addressed by studying siderophile element systematics in lunar samples in conjunction with the experimentally

Table 1  
Measured starting compositions of silicate melt (in wt.%) obtained with EPMA.

	<i>N</i>	SiO <sub>2</sub>	FeO	MgO	CaO	Al <sub>2</sub> O <sub>3</sub>	TiO <sub>2</sub>	Cr <sub>2</sub> O <sub>3</sub>	MnO	K <sub>2</sub> O	Total
A14BG <sup>a</sup>	17	32.1(1)	23.3(1)	12.2(0)	7.0(0)	4.8(0)	18.9(1)	0.96(1)	0.33(1)	0.1(0)	99.8(1)
A14YG <sup>a,b</sup>	–	–	–	–	–	–	–	–	–	–	–
A15GG <sup>a</sup>	17	48.3(1)	15.6(6)	17.2(4)	8.9(0)	7.3(0)	0.25(1)	0.53(1)	0.19(1)	–	98.3(1)
A17OG <sup>a</sup>	25	37.4(3)	21.0(2)	11.1(2)	8.7(0)	8.1(2)	10.1(5)	0.72(1)	0.32(2)	0.013(4)	97.7(1)
LBS10 <sup>c</sup>	25	48.2(3)	16.8(1)	4.37(2)	9.91(2)	10.9(1)	6.7(1)	–	–	0.015(3)	97.1(1)

<sup>a</sup> Composition after Delano (1986a).

<sup>b</sup> The Apollo 14 yellow glass (A14YG) starting composition was not measured.

<sup>c</sup> Composition after Lin et al. (2017).

Table 2  
Overview of experimental run conditions.

Run <sup>a</sup>	P (GPa)	T(K)	Time (h)	Starting composition	Capsule	$\Delta IW$ <sup>b</sup>	$\gamma_{Fe}^{sulfide}$ <sup>c</sup>	$\Delta IW$ <sup>d</sup>	Phases and modal abundances	$x_{FeS}^{sulfide}$	SCSS (ppm) <sup>e</sup>
A14BGAM-1 <sup>f,g</sup>	1.0	1783	1	A14BG + FeS	MgO	–	–	–	sul(20)+ol(35)+gl(25)+quench(20)	–	5275(429)
A14BGAM-2 <sup>f,g</sup>	1.0	1783	1	A14BG + FeS	MgO	–1.28	1.61	–1.69	sul(20)+ol(25)+gl(30)+quench(25)	0.91	5473(865)
A14BG-3	1.0	1683	1.5	A14BG + FeS	C	–1.23	1.84	–1.76	sul(50)+opx(10)+gl(40)	0.92	4755(84)
A14BG-4	1.5	1683	1.5	A14BG + FeS	C	–0.82	1.86	–1.36	sul(50)+opx(10)+quench(40)	0.88	6273(686)
A14BG-5	2.0	1683	1.5	A14BG + FeS	C	–0.60	1.89	–1.15	sul(50)+opx(15)+quench(35)	0.85	7343(1642)
A14BG-6	2.5	1683	1.5	A14BG + FeS	C	–0.67	1.91	–1.24	sul(50)+ol(15)+opx(15)+quench(20)	0.86	7384(1805)
A14YG1-14	1.0	1683	1	A14YG + FeS	C	–1.49	1.76	–1.98	sul(50)+ol(15)+gl(35)	0.92	2377(206)
A14YG1-15A	1.0	1783	1	A14YG + FeS	C	–1.18	1.68	–1.63	sul(40)+gl(60)	0.90	3644(188)
A14YG1-15B	1.0	1783	0.5	A14YG + FeS	C	–0.94	1.69	–1.39	sul(15)+gl(85)	0.87	4465(388)
A14YG1-15C	1.0	1783	2	A14YG + FeS	C	–1.41	1.67	–1.86	sul(60)+gl(40)	0.92	2928(156)
A14YG1.5-15	1.5	1783	1	A14YG + FeS	C	–1.43	1.69	–1.89	sul(20)+gl(80)	0.92	3381(315)
A14YG2-15	2.0	1783	1	A14YG + FeS	C	–0.89	1.71	–1.36	sul(50)+gl(50)	0.87	3658(285)
A14YG2.5-15	2.5	1783	1	A14YG + FeS	C	–0.89	1.69	–1.35	sul(50)+gl(25)+quench(25)	0.87	2677(166)
A15GGAM-1 <sup>g</sup>	1.0	1783	1	A15GG + FeS	MgO	–	–	–	sul(10)+ol(25)+gl(40)+quench(25)	–	2043(111)
A15GGAM-2B <sup>g</sup>	1.0	1783	1	A15GG + FeS	MgO	–1.71	1.59	–2.11	sul(20)+ol(25)+gl(35)+quench(20)	0.94	2049(164)
A15GG-1	1.0	1783	2	A15GG + FeS	C	–1.68	1.76	–2.17	sul(50)+ol(5)+gl(45)	0.92	2206(52)
A15GG-5	2.0	1783	1	A15GG + FeS	C	–1.00	1.70	–1.46	sul(40)+ol(20)+gl(20)+quench(20)	0.94	2567(1052)
A15GG-6	2.5	1783	1	A15GG + FeS	C	–1.32	1.75	–1.80	sul(40)+ol(25)+gl(20)+quench(15)	0.93	2106(600)
A17OG-1	1.0	1683	1	A17OG + FeS	C	–1.42	1.77	–1.91	sul(50)+gl(50)	0.93	2533(64)
A17OG-2	1.0	1764	1	A17OG + FeS	C	–1.47	1.67	–1.92	sul(50)+gl(50)	0.93	3034(83)
A17OG-3	1.0	1783	1	A17OG + FeS	C	–1.32	1.68	–1.77	sul(60)+gl(40)	0.92	3005(55)
A17OG-4	1.0	1883	0.5	A17OG + FeS	C	–1.51	1.59	–1.92	sul(50)+gl(50)	0.93	4130(89)
A17OG-5	1.5	1783	1	A17OG + FeS	C	–0.85	1.68	–1.30	sul(40)+gl(60)	0.88	4555(739)
A17OG-6	2.0	1783	1	A17OG + FeS	C	–0.96	1.72	–1.43	sul(40)+gl(60)	0.88	3199(205)
A17OG-7	2.5	1783	1	A17OG + FeS	C	–0.79	1.87	–1.54	sul(50)+gl(50)	0.82	2388(193)
LBS1-14	1.0	1683	2	LBS10 + FeS	C	–2.21	1.76	–2.70	sul(15)+gl(85)	0.96	1882(56)
LBS1-15	1.0	1783	1	LBS10 + FeS	C	–1.41	1.65	–1.85	sul(20)+gl(80)	0.93	2336(78)
LBS1-155	1.0	1833	1	LBS10 + FeS	C	–1.79	1.59	–2.20	sul(50)+gl(50)	0.94	2417(185)
LBS1.5-15	1.5	1783	1	LBS10 + FeS	C	–0.95	1.71	–1.42	sul(50)+gl(50)	0.88	2872(66)
LBS2-15	2.0	1783	1	LBS10 + FeS	C	–0.91	1.69	–1.37	sul(20)+gl(80)	0.89	2595(287)

<sup>a</sup> A14BG = Apollo 14 black glass, A14YG = Apollo 14 yellow glass, A15GG = Apollo 15 green glass, A17OG = Apollo 17 orange glass, LBS = step LBS10 (Lin et al., 2017).

<sup>b</sup> Assuming ideal mixing behavior of Fe.

<sup>c</sup> Calculated using the thermodynamic model for Fe-S alloys from Lee and Morita (2002) and assuming a reciprocal temperature dependency of  $\gamma_{Fe}^{sulfide}$  (Wood et al., 2014).

<sup>d</sup> Assuming non-ideal mixing behavior of Fe.

<sup>e</sup> Numbers in parentheses represents 2 standard errors (SE).

<sup>f</sup> Sulfides were dispersed as small flecks, making EMPA and/or LA-ICP-MS analyses of sulfide phase impossible.

<sup>g</sup> Experiments performed in MgO capsules may have suffered significant H<sub>2</sub>O contamination from dehydration of the talc-Pyrex cell (e.g., Vander Kaaden et al., 2015) and are only reported for comparison purposes (i.e. the values were not considered in subsequent regressions).

Table 3

Major and minor element composition of silicate melts determined by EPMA and LA-ICP-MS. Numbers in parentheses represent 2 SE.

Run # EPMA	A14BGAM-1 N = 25 <sup>a</sup>	A14BGAM-2 N = 32	A14BG-3 N = 25	A14BG-4 N = 29	A14BG-5 N = 15	A14BG-6 N = 14	A14YG1-14 N = 10	A14YG1-15A N = 10	A14YG1-15B N = 20	A14YG1-15C N = 21	A14YG1.5-15 N = 9
<i>Silicate melt</i>											
SiO <sub>2</sub> (wt.%)	24.14(33)	28.32(32)	37.94(6)	34.18(14)	30.80(40)	33.23(128)	45.77(28)	45.18(35)	42.35(37)	47.31(21)	47.36(9)
TiO <sub>2</sub>	25.33(50)	20.21(55)	18.77(4)	17.79(12)	18.05(36)	14.28(89)	6.53(8)	4.99(4)	4.90(6)	5.17(8)	4.39(7)
Al <sub>2</sub> O <sub>3</sub>	6.34(12)	6.16(18)	5.45(2)	5.20(6)	5.04(9)	4.71(18)	9.15(8)	6.89(5)	6.70(3)	7.29(3)	6.59(13)
Cr <sub>2</sub> O <sub>3</sub>	0.33(4)	0.62(3)	0.27(1)	0.36(1)	0.34(2)	0.34(4)	0.15(2)	0.26(3)	0.22(1)	0.18(1)	0.12(2)
FeO	11.75(28)	13.17(26)	12.21(6)	18.59(13)	22.96(40)	20.85(41)	9.93(10)	14.20(11)	18.44(10)	11.19(5)	10.48(15)
MnO	0.26(1)	0.25(1)	0.20(1)	0.25(1)	0.27(1)	0.27(1)	0.22(2)	0.26(2)	0.28(1)	0.25(2)	0.21(3)
MgO	8.53(70)	14.41(115)	13.89(4)	12.01(22)	10.47(55)	12.32(110)	13.74(9)	16.21(7)	15.22(5)	17.05(7)	16.13(53)
CaO	19.91(54)	13.96(60)	7.62(1)	7.38(6)	7.07(25)	6.22(54)	10.64(9)	8.41(5)	8.32(6)	8.86(5)	8.95(8)
Na <sub>2</sub> O	0.35(1)	0.26(2)	0.21(1)	0.22(2)	0.19(2)	1.88(20)	0.57(2)	0.62(3)	0.45(2)	0.47(1)	0.88(11)
K <sub>2</sub> O	0.20(1)	0.15(1)	0.138(3)	0.16(1)	0.17(6)	0.09(2)	0.28(1)	0.10(1)	0.13(1)	0.10(1)	0.77(7)
S (ppm)	5275(429)	5473(865)	4755(84)	6273(686)	7343(1642)	7384(1805)	2377(206)	3644(188)	4465(388)	2928(156)	3381(315)
Total	98.45(18)	98.88(23)	97.90(11)	97.72(17)	97.21(70)	96.03(93)	97.57(40)	98.03(31)	97.42(23)	98.08(23)	96.73(30)
LA-ICP-MS	N = 4	N = 7	N = 6	N = 6	n.a. <sup>c</sup>	N = 4	N = 5	N = 6	N = 4	N = 4	N = 6
CaO (wt.%)	15.39(354)	14.46(33)	7.84(19)	7.09(6)	–	6.60(59)	10.73(22)	9.05(5)	8.74(11)	9.31(13)	9.60(17)
TiO <sub>2</sub>	23.71(454)	23.43(38)	20.50(49)	18.23(14)	–	16.15(89)	7.11(17)	5.58(1)	5.37(6)	5.66(5)	4.90(8)
V (ppm)	32(3)	41(1)	17.7(5)	18.3(2)	–	20(1)	15(1)	13.0(1)	15.9(1)	14.1(3)	19(1)
Cr	3695(397)	4992(171)	1927(36)	2264(26)	–	2232(222)	991(42)	1825(18)	1586(30)	1295(34)	833(16)
Mn	1957(197)	2067(45)	1715(38)	1770(19)	–	2108(104)	1668(18)	2083(15)	2051(34)	1891(50)	1599(20)
Ni	1.33(47)	1.08(15)	b.d.l. <sup>b</sup>	b.d.l.	–	b.d.l.	b.d.l.	b.d.l.	b.d.l.	b.d.l.	b.d.l.
Co	0.19(6)	0.41(5)	0.46(4)	0.73(4)	–	0.89(8)	0.36(3)	0.59(4)	0.86(5)	0.49(2)	0.49(5)
Cu	25(3)	4.6(5)	1.56(20)	1.92(19)	–	3.0(4)	0.95(12)	1.30(11)	2.5(1)	1.06(3)	1.07(6)
Zn	74(9)	51(2)	29(1)	61(1)	–	105(11)	173(13)	51(1)	94(1)	43(3)	24.7(5)
Ga	6.3(12)	6.8(1)	9.0(4)	10.6(2)	–	9.5(6)	8.9(6)	5.7(1)	8.7(1)	7.3(3)	11.9(4)
Ge	1.22(12)	1.67(7)	7.6(4)	18.5(3)	–	30(1)	6.0(5)	4.2(3)	15.9(3)	4.4(2)	7.2(4)
As	b.d.l.	b.d.l.	2.3(4)	4.9(7)	–	11(3)	2.0(3)	1.79(27)	3.4(4)	1.40(50) <sup>d</sup>	2.5(5)
Se	45(7)	52(3)	25(2)	31(2)	–	34(1)	16(3)	24(1)	41(3)	22(1)	17(1)
Mo	0.13(8)	1.72(17)	4.3(3)	13.6(3)	–	16(2)	3.3(6)	6.5(2)	12.7(6)	4.2(2)	6.8(3)
Sn	1.95(26)	3.0(1)	2.4(2)	4.2(2)	–	9.5(16)	1.39(10)	2.45(7)	4.8(2)	1.50(8)	1.72(8)
Sb	b.d.l.	b.d.l.	0.29(4)	0.69(5)	–	1.46(53)	0.17(1)	0.31(3)	0.63(4)	0.23(2)	0.28(2)
Te	18(1)	12(1)	3.0(2)	3.7(4)	–	6.2(9)	1.20(37)	2.6(1)	7.6(5)	1.60(24)	1.39(20)
W	5.4(12)	7.0(3)	3.4(2)	3.9(1)	–	2.8(7)	13(1)	5.9(1)	4.5(2)	2.6(1)	14(1)
Pb	1.67(17)	0.85(6)	0.14(4)	0.29(2)	–	0.80(23)	0.16(2)	0.25(1)	0.37(4)	0.18(2)	0.08(2)
Run # EPMA	A14YG2-15 N = 10	A14YG2.5-15 N = 5	A17OG-1 N = 45	A17OG-2 N = 44	A17OG-3 N = 50	A17OG-4 N = 35	A17OG-5 N = 20	A17OG-6 N = 20	A17OG-7 N = 20	LBS1-14 N = 33	LBS1-15 N = 33
<i>Silicate melt</i>											
SiO <sub>2</sub> (wt.%)	40.87(35)	40.87(262)	47.10(24)	47.81(30)	47.16(34)	48.26(76)	40.23(56)	42.93(35)	41.64(44)	53.04(38)	49.81(25)
TiO <sub>2</sub>	5.56(6)	4.38(98)	9.65(4)	9.43(4)	9.36(3)	9.50(6)	5.87(22)	8.96(8)	9.77(11)	7.44(3)	6.79(5)
Al <sub>2</sub> O <sub>3</sub>	7.40(6)	6.43(43)	7.96(2)	8.04(3)	7.90(3)	8.30(4)	8.42(15)	7.61(4)	7.85(4)	12.39(4)	11.68(3)
Cr <sub>2</sub> O <sub>3</sub>	0.23(1)	0.25(4)	0.14(1)	0.10(1)	0.20(1)	0.18(1)	0.29(2)	0.35(1)	0.42(1)	b.d.l.	b.d.l.

FeO	18.75(13)	19.40(141)	10.61(5)	10.00(5)	11.81(10)	9.50(7)	17.38(37)	16.61(9)	17.04(12)	4.02(12)	10.12(12)
MnO	0.30(2)	0.23(2)	0.17(1)	0.15(1)	0.20(1)	0.18(1)	0.17(2)	0.26(2)	0.29(1)	0.02(1)	0.017(4)
MgO	13.49(16)	16.41(246)	12.34(4)	12.25(10)	11.78(5)	12.19(18)	8.14(27)	10.62(6)	9.54(6)	5.12(5)	4.68(6)
CaO	9.23(9)	8.27(166)	8.83(3)	8.84(3)	8.70(2)	8.89(4)	5.34(12)	8.42(7)	8.94(9)	11.65(6)	10.98(3)
Na <sub>2</sub> O	0.47(2)	0.29(7)	0.41(1)	0.51(1)	0.37(1)	0.71(2)	2.41(6)	0.74(2)	0.45(1)	0.22(1)	0.23(1)
K <sub>2</sub> O	0.13(2)	0.10(4)	0.100(2)	0.37(1)	0.024(2)	0.027(3)	0.16(1)	0.03(1)	0.04(1)	0.24(2)	0.19(3)
S (ppm)	3658(285)	2677(166)	2533(64)	3034(83)	3005(55)	4130(89)	4555(739)	3199(205)	2388(193)	1882(56)	2336(78)
Total	97.35(38)	96.75(177)	97.95(16)	98.26(20)	98.24(17)	98.78(43)	89.56(59) <sup>c</sup>	97.32(29)	96.13(42)	94.67(27)	95.08(44)
LA-ICP-MS	<i>N</i> = 4	<i>n. a.</i>	<i>N</i> = 4	<i>N</i> = 4	<i>N</i> = 3	<i>N</i> = 4	<i>N</i> = 4	<i>N</i> = 4	<i>N</i> = 3	<i>N</i> = 3	<i>N</i> = 4
CaO (wt.%)	9.56(14)	–	9.49(9)	9.25(18)	8.95(2)	9.30(6)	5.77(13)	8.81(10)	9.34(6)	12.46(17)	11.02(41)
TiO <sub>2</sub>	6.14(11)	–	10.91(17)	10.51(21)	10.01(11)	10.48(5)	7.01(2)	9.78(8)	10.56(9)	7.95(12)	6.94(16)
V (ppm)	17(1)	–	15(3)	13.9(4)	13.6(5)	10.9(2)	8.7(1)	14.4(2)	13.6(1)	7.6(2)	8.3(4)
Cr	1641(59)	–	1111(28)	744(20)	1369(18)	1313(22)	2107(27)	2423(44)	3006(34)	34(2)	65(3)
Mn	2151(43)	–	1500(20)	1226(31)	1626(24)	1513(13)	1430(25)	1994(16)	2066(17)	124(2)	159(10)
Co	0.85(8)	–	0.49(3)	0.45(5)	0.45(6)	0.39(2)	0.88(4)	0.75(7)	0.94(6)	0.16(4) <sup>d</sup>	0.34(2)
Ni	0.67(4)	–	b.d.l.	b.d.l.	b.d.l.	b.d.l.	b.d.l.	b.d.l.	1.26(23)	b.d.l.	b.d.l.
Cu	2.4(4)	–	1.12(13)	1.27(21)	1.22(8)	1.82(15)	1.38(25)	1.88(26)	3.1(9)	0.66(25)	1.23(7)
Zn	58(1)	–	24(1)	64(2)	30(2)	27(1)	28(1)	64(4)	76(1)	45(4)	87(7)
Ga	12.2(3)	–	11.2(4)	10.5(5)	8.5(2)	3.9(2)	3.6(2)	8.3(2)	7.1(1)	5.7(4)	5.1(3)
Ge	15(1)	–	11(1)	7.0(4)	7.6(3)	1.75(25)	b.d.l.	8.6(5)	6.1(3)	2.3(3)	3.3(3)
As	6.5(6)	–	2.1(5)	2.5(4)	1.61(56) <sup>d</sup>	1.96(25)	b.d.l.	2.2(4)	b.d.l.	3.0(5)	3.5(8)
Se	25(3)	–	17(3)	21(4)	25(2)	25(2)	44(2)	19(3)	13(4)	8.2(8)	16(2)
Mo	19(1)	–	2.8(1)	2.5(2)	3.20(3)	1.59(10)	4.8(3)	8.7(5)	9.8(3)	0.46(10)	2.5(2)
Sn	4.1(3)	–	2.6(2)	1.84(7)	1.83(5)	1.66(10)	1.36(10)	3.8(2)	1.83(1)	1.45(10)	2.5(1)
Sb	0.85(7)	–	0.25(3)	0.19(2)	0.19(2)	0.10(1)	b.d.l.	0.45(5)	0.11(1)	0.64(6)	0.63(4)
Te	3.2(4)	–	1.24(12)	2.7(3)	2.5(2)	2.8(3)	1.91(19)	1.28(22)	0.38(15)	0.65(18)	1.78(39) <sup>d</sup>
W	3.2(2)	–	4.2(2)	11.5(5)	6.2(2)	3.8(1)	6.1(2)	5.4(3)	2.5(4)	4.3(1)	4.1(2)
Pb	0.207(1)	–	0.11(3)	0.15(2)	0.13(6)	0.17(3)	0.79(6)	0.35(2)	0.60(10)	1.43(19)	2.1(3)
Run #	LBS1-155	LBS1.5–15	LBS2-15	A15GGAM-1	A15GGAM-2B	A15GG-1	A15GG-5	A15GG-6			
EPMA	<i>N</i> = 10	<i>N</i> = 41	<i>N</i> = 7	<i>N</i> = 37	<i>N</i> = 25	<i>N</i> = 25	<i>N</i> = 16	<i>N</i> = 21			
<i>Silicate melt</i>											
SiO <sub>2</sub> (wt.%)	53.59(29)	47.64(25)	46.77(39)	48.64(20)	49.41(15)	52.18(11)	46.17(154)	49.62(65)			
TiO <sub>2</sub>	7.02(6)	6.35(4)	6.27(13)	0.27(1)	0.28(1)	0.28(1)	0.20(5)	0.22(3)			
Al <sub>2</sub> O <sub>3</sub>	12.57(8)	10.94(2)	10.77(5)	8.95(11)	8.60(12)	9.04(13)	6.88(100)	7.54(82)			
Cr <sub>2</sub> O <sub>3</sub>	0.02(1)	0.02(1)	0.02(1)	0.37(1)	0.37(1)	0.23(2)	0.23(5)	0.32(6)			
FeO	6.55(8)	16.27(6)	17.47(17)	4.80(10)	8.50(12)	7.33(16)	17.01(101)	11.50(12)			
MnO	0.05(1)	0.05(1)	0.06(2)	0.18(1)	0.18(1)	0.15(1)	0.19(1)	0.18(1)			
MgO	5.10(7)	4.50(4)	4.31(5)	20.29(41)	17.72(38)	16.07(9)	17.51(227)	19.32(161)			
CaO	11.89(6)	10.31(4)	10.12(8)	11.66(17)	11.27(18)	9.77(14)	7.44(127)	7.59(86)			
Na <sub>2</sub> O	0.08(1)	0.11(1)	0.09(1)	0.051(4)	0.04(1)	0.08(1)	0.26(8)	0.09(2)			
K <sub>2</sub> O	0.08(2)	0.040(2)	0.02(1)	0.018(1)	0.020(2)	0.035(2)	0.02(1)	0.03(1)			
S (ppm)	2417(185)	2872(66)	2595(287)	2043(111)	2049(164)	2206(52)	2567(1052)	2106(600)			
Total	97.53(31)	96.94(19)	96.55(56)	95.74(20)	96.91(21)	95.72(14)	96.54(55)	96.94(49)			

(continued on next page)

Table 3 (continued)

LA-ICP-MS	<i>N</i> = 2	<i>N</i> = 4	<i>N</i> = 2	<i>N</i> = 7	<i>N</i> = 7	<i>N</i> = 5	<i>N</i> = 5	<i>N</i> = 1
CaO (wt.%)	12.65(21)	10.47(9)	10.80(25)	13.18(20)	10.34(103)	9.38(4)	10.18(146)	8.10(22)
TiO <sub>2</sub>	7.99(13)	6.54(4)	6.91(32)	0.327(4)	0.27(3)	0.282(3)	0.32(1)	0.231(2)
V (ppm)	10.9(3)	13(1)	13.6(1)	9.7(4)	9.6(5)	8.4(3)	24(2)	17(1)
Cr	49(1)	106(4)	133(5)	2934(36)	2422(107)	1623(27)	1274(32)	1497(124)
Mn	326(6)	431(12)	464(20)	1563(14)	1538(54)	1202(16)	1924(34)	1238(77)
Co	0.33(24)	0.67(4)	0.63(15)	b.d.l.	0.19(4)	0.29(6)	1.03(6)	0.51(7)
Ni	b.d.l.	b.d.l.	1.03(15)	b.d.l.	1.49(19)	b.d.l.	1.62(79)	b.d.l.
Cu	1.32(31)	1.38(16)	1.53(59)	1.23(30)	2.1(3)	0.49(10)	2.8(3)	0.30(13)
Zn	14(2)	70(2)	44(6)	55(2)	51(5)	34(1)	67(4)	31(2)
Ga	8.2(1)	11(1)	10.0(3)	5.5(2)	4.9(5)	5.6(1)	20(1)	8.1(5)
Ge	2.9(8)	13(1)	10.3(3)	b.d.l.	0.64(8)	1.54(22)	28(2)	9.3(8)
As	b.d.l.	4.0(6)	b.d.l.	b.d.l.	3.1(5)	b.d.l.	2.5(3)	b.d.l.
Se	11(3)	21(4)	18(5)	20(4)	16(2)	13(2)	20(2)	7.7(41)
Mo	1.11(15)	4.0(4)	1.93(5)	0.07(1)	1.88(51)	1.05(12)	18(1)	2.9(3)
Sn	1.04(11)	6.8(4)	7.8(2)	0.65(9)	1.16(17)	1.05(10)	4.8(4)	0.66(10)
Sb	0.54(4)	0.96(8)	0.78(5)	b.d.l.	0.56(17)	0.20(5)	0.56(6)	b.d.l.
Te	1.42(30)	3.0(5)	2.5(5)	4.9(18)	16(4)	0.35(1) <sup>c</sup>	1.9(7)	1.9(4)
W	9.7(3)	3.4(5)	3.8(2)	0.22(13)	2.7(3)	3.2(1)	8.8(9)	4.7(4)
Pb	0.33(1)	1.01(1)	1.33(1)	0.80(5)	0.44(5)	0.48(6)	0.36(14)	b.d.l.

<sup>a</sup> *N* = number of analyses.<sup>b</sup> b.d.l. = below detection limit.<sup>c</sup> n.a. = not analyzed.<sup>d</sup> Close to detection limit.<sup>e</sup> Low total is due to highly porous texture of the silicate melt in this experiment.

Table 4

Major and minor element composition of the sulfide melts determined by EPMA and LA-ICP-MS. Numbers in parentheses represent 2 SE.

Run #	A14BGAM-1 <sup>a</sup>	A14BGAM-2	A14BG-3	A14BG-4	A14BG-5	A14BG-6	A14YG1-14	A14YG1-15	A14YG1-15B	A14YG1-15C	A14YG1.5-15
EPMA	<i>n.a.</i> <sup>b</sup>	<i>N = 6</i> <sup>c</sup>	<i>N = 22</i>	<i>N = 20</i>	<i>N = 25</i>	<i>N = 24</i>	<i>N = 5</i>	<i>N = 3</i>	<i>N = 3</i>	<i>N = 10</i>	<i>N = 5</i>
<i>Sulfide</i>											
Fe (wt.%)	–	67.38(177)	61.17(18)	59.82(46)	59.81(47)	60.28(53)	60.55(61)	59.08(91)	60.31(57)	60.84(24)	56.97(55)
S	–	32.39(260)	38.69(27)	36.04(45)	35.36(39)	38.21(61)	33.42(54)	31.68(57)	31.07(70)	33.15(47)	32.57(48)
Ca	–	0.08(2)	0.008(4)	0.01(1)	0.009(4)	b.d.l. <sup>d</sup>	b.d.l.	0.03(4)	0.03(4)	0.01(1)	0.02(4)
Ti	–	0.21(3)	0.08(4)	0.11(4)	0.07(3)	0.005(3)	0.05(2)	0.04(4)	0.08(8)	0.04(2)	0.03(1)
Cr	–	0.05(1)	0.25(4)	0.20(4)	0.10(2)	0.095(5)	0.21(2)	0.27(12)	0.18(6)	0.25(2)	0.16(2)
Mn	–	0.04(1)	0.09(1)	0.07(1)	0.07(1)	0.03(1)	0.12(1)	0.12(3)	0.07(1)	0.13(1)	0.09(1)
Se	–	0.41(3)	0.53(2)	0.52(3)	0.55(1)	0.48(1)	0.49(3)	0.43(5)	0.46(6)	0.47(2)	0.43(5)
Te	–	0.43(16)	0.36(5)	0.31(6)	0.30(8)	0.13(1)	0.14(6)	0.17(6)	0.40(6)	0.19(6)	0.22(5)
Pt	–	–	0.23(9)	1.36(64)	1.99(67)	0.39(5)	1.31(107)	0.84(51)	0.30(25)	0.75(22)	1.45(55)
Total	–	101.03(78)	101.42(24)	98.48(69)	98.28(54)	97.12(132)	96.32(32)	92.72(115)	93.13(49)	95.86(47)	92.04(112)
O (wt.%) <sub>calc</sub> <sup>e</sup>	–	3.16	2.93	4.46	5.51	5.00	2.38	3.41	4.43	2.69	2.52
LA-ICP-MS	<i>n.a.</i>	<i>n.a.</i>	<i>N = 3</i>	<i>N = 4</i>	<i>N = 2</i>	<i>N = 3</i>	<i>N = 3</i>	<i>N = 4</i>	<i>n.a.</i>	<i>N = 4</i>	<i>n.a.</i>
Pt (wt.%)	–	–	0.51(11)	1.35(24)	1.78(47)	2.79(18)	1.08(6)	1.42(17)	–	1.05(24)	–
Si (ppm)	–	–	552(153)	517(34)	515(116)	287(41)	470(23)	502(22)	–	616(80)	–
Ca	–	–	413(67)	294(69)	359(75)	169(19)	473(165)	524(38)	–	909(157)	–
Ti	–	–	927(200)	1026(76)	867(91)	339(42)	431(16)	490(85)	–	496(27)	–
V	–	–	5.1(7)	4.2(2)	3.7(1)	1.79(24)	6.0(2)	4.2(5)	–	5.9(2)	–
Cr	–	–	<i>Int.</i> <sup>f</sup>	<i>Int.</i>	<i>Int.</i>	<i>Int.</i>	1773(46)	2425(184)	–	<i>Int.</i>	–
Mn	–	–	1090(87)	861(54)	634(84)	413(37)	<i>Int.</i>	<i>Int.</i>	–	1513(76)	–
Co	–	–	24(2)	29(2)	23(3)	16(1)	21(1)	20.5(4)	–	22(1)	–
Ni	–	–	254(22)	306(22)	283(39)	246(15)	205(11)	202(6)	–	205(12)	–
Cu	–	–	497(42)	614(38)	554(93)	773(67)	510(26)	331(12)	–	411(20)	–
Zn	–	–	73(6)	90(4)	61(6)	65(7)	524(19)	88(7)	–	112(11)	–
Ga	–	–	0.95(20)	0.58(10)	0.51(11)	0.17(3)	0.77(2)	0.44(8)	–	0.74(13)	–
Ge	–	–	10.0(12)	6.7(5)	7.1(1)	3.2(3)	5.8(2)	4.2(5)	–	5.9(6)	–
As	–	–	88(10)	64(7)	98(3)	87(3)	51(4)	59(4)	–	56(4)	–
Se	–	–	3697(348)	4292(200)	4370(498)	3826(369)	4075(198)	3547(118)	–	4473(298)	–
Mo	–	–	172(16)	174(15)	92(11)	41(3)	125(3)	103(2)	–	134(3)	–
Sn	–	–	31(6)	26(2)	33(4)	29(1)	14.8(5)	18(2)	–	16(1)	–
Sb	–	–	8.2(20)	6.3(9)	9.4(4)	7.5(1)	3.02(4)	4.7(5)	–	4.6(5)	–
Te	–	–	6062(224)	5197(827)	4297(594)	7667(212)	2504(209)	2865(115)	–	3414(432)	–
W	–	–	0.10(2)	0.09(4)	0.06(2)	0.033(2)	0.33(11)	0.18(2)	–	0.12(3)	–
Pb	–	–	3.9(3)	6.2(13)	4.5(16)	7.8(10)	5.3(5)	6.5(5)	–	8.0(6)	–

Run # EPMA	A14YG2-15 <i>N</i> = 5	A14YG2.5-15 <i>N</i> = 9	A17OG-1 <i>N</i> = 35	A17OG-2 <i>N</i> = 32	A17OG-3 <i>N</i> = 30	A17OG-4 <i>N</i> = 30	A17OG-5 <i>N</i> = 10	A17OG-6 <i>N</i> = 10	A17OG-7 <i>N</i> = 10	LBS1-14 <i>N</i> = 6	LBS1-15 <i>N</i> = 12
<i>Sulfide</i>											
Fe (wt.%)	60.46(60)	61.43(36)	62.10(25)	62.00(35)	62.19(33)	61.12(42)	62.15(25)	58.95(53)	43.66(152)	57.48(191)	61.75(32)
S	32.13(27)	31.26(54)	35.01(27)	34.75(17)	34.40(33)	35.04(27)	31.90(30)	33.36(32)	28.71(147)	33.75(79)	33.16(66)
Ca	b.d.l.	b.d.l.	0.01(1)	0.01(1)	0.02(1)	0.03(1)	0.01(3)	b.d.l.	b.d.l.	b.d.l.	0.01(1)
Ti	0.05(3)	0.03(2)	0.03(1)	0.06(2)	0.08(2)	0.05(3)	0.05(1)	0.04(1)	0.01(1)	0.04(1)	0.04(2)
Cr	0.13(2)	0.05(1)	0.16(2)	0.18(3)	0.26(3)	0.30(5)	0.23(3)	0.21(3)	0.13(3)	0.02(1)	0.01(1)
Mn	0.09(1)	0.07(1)	0.087(4)	0.09(1)	0.09(1)	0.12(1)	0.06(1)	0.07(1)	0.04(1)	0.02(1)	0.01(1)
Se	0.47(5)	0.51(3)	0.47(1)	0.49(1)	0.51(1)	0.53(2)	0.56(2)	0.47(3)	0.40(7)	0.36(5)	0.39(3)
Te	0.42(6)	0.33(14)	0.22(3)	0.36(5)	0.33(5)	0.30(5)	0.15(1)	0.15(5)	0.25(14)	0.18(6)	0.15(5)
Pt	1.90(66)	1.02(49)	0.47(15)	0.42(12)	0.71(25)	1.34(42)	0.12(4)	2.42(49)	20.52(276)	3.08(67)	0.73(39)
Total	95.66(29)	94.74(51)	98.59(51)	98.38(39)	98.60(61)	99.01(42)	95.27(36)	95.69(66)	93.79(49)	94.98(145)	96.26(43)
O (wt.%) <sub>calc</sub>	4.50	4.66	2.55	2.40	2.83	2.28	4.33	3.99	4.09	0.96	2.43
LA-ICP-MS	<i>N</i> = 4	<i>n.a.</i>	<i>N</i> = 4	<i>N</i> = 4	<i>N</i> = 3	<i>N</i> = 4	<i>N</i> = 4	<i>N</i> = 4	<i>N</i> = 4	<i>n.a.</i>	<i>n.a.</i>
Pt (wt.%)	1.51(15)	–	0.36(3)	0.42(3)	0.86(5)	1.81(32)	0.09(1)	3.24(6)	16.74(118)	–	–
Si (ppm)	519(30)	–	506(100)	867(236)	641(87)	569(51)	734(48)	731(54)	528(126)	–	–
Ca	251(18)	–	312(54)	728(250)	391(69)	645(62)	360(35)	562(85)	316(76)	–	–
Ti	619(87)	–	520(49)	881(260)	726(147)	899(245)	761(39)	515(39)	164(8)	–	–
V	5.1(7)	–	4.3(2)	7.0(4)	5.8(7)	6.1(3)	2.4(1)	3.3(3)	1.2(1)	–	–
Cr	1437(124)	–	<i>Int.</i>	<i>Int.</i>	<i>Int.</i>	<i>Int.</i>	<i>Int.</i>	<i>Int.</i>	<i>Int.</i>	–	–
Mn	<i>Int.</i>	–	768(32)	1038(13)	1131(49)	1254(82)	603(49)	865(59)	388(32)	–	–
Co	24.6(3)	–	20(1)	23(1)	25(2)	19(1)	26(2)	26(1)	22(2)	–	–
Ni	235(1)	–	201(7)	226(5)	246(16)	198(13)	317(24)	289(11)	243(21)	–	–
Cu	401(7)	–	305(14)	428(7)	466(30)	378(31)	386(32)	512(30)	463(43)	–	–
Zn	57(1)	–	42(3)	154(9)	73(8)	76(13)	32(3)	70(5)	49(4)	–	–
Ga	0.62(11)	–	0.73(9)	1.43(8)	0.85(9)	0.70(2)	0.15(3)	0.34(6)	0.12(2)	–	–
Ge	4.5(4)	–	7.7(9)	13(1)	8.7(7)	5.2(9)	1.45(34)	4.2(6)	4.2(5)	–	–
As	61(2)	–	49(2)	75(4)	63(9)	53(7)	2.4(6)	47(5)	29(8)	–	–
Se	4016(40)	–	3301(100)	4748(82)	5032(432)	4255(334)	3825(318)	4725(319)	4015(843)	–	–
Mo	143(4)	–	112(4)	154(7)	162(12)	116(7)	63(6)	141(2)	79(5)	–	–
Sn	20(1)	–	18(1)	20(2)	15(2)	14(2)	3.6(3)	21(3)	7.6(15)	–	–
Sb	6.1(4)	–	3.4(1)	4.7(2)	5.1(9)	3.3(5)	3.5(4)	5.9(6)	2.8(5)	–	–
Te	3856(225)	–	1610(83)	4255(315)	4171(684)	3310(490)	1089(84)	3510(504)	3269(1264)	–	–
W	0.07(1)	–	0.13(2)	0.97(30)	0.29(2)	0.41(8)	0.16(3)	0.15(4)	0.03(1)	–	–
Pb	2.8(2)	–	2.0(1)	2.5(3)	2.8(4)	3.6(7)	8.3(7)	5.2(9)	8.0(29)	–	–
Run # EPMA	LBS1-155 <i>N</i> = 15	LBS1.5–15 <i>N</i> = 21	LBS2-15 <i>N</i> = 5	A15GGAM-1 <i>n.a.</i>	A15GGAM-2B <i>N</i> = 8	A15GG-1 <i>N</i> = 12	A15GG-5 <i>N</i> = 22	A15GG-6 <i>N</i> = 11			
<i>Sulfide</i>											
Fe (wt.%)	58.90(30)	61.66(50)	61.79(60)	–	66.20(146)	55.09(71)	59.00(73)	56.60(119)			
S	34.61(20)	32.58(47)	32.64(27)	–	32.30(201)	36.07(30)	36.40(43)	37.66(37)			
Ca	0.01(1)	b.d.l.	b.d.l.	–	0.07(4)	0.02(1)	0.01(1)	0.02(1)			
Ti	0.06(1)	0.04(2)	0.03(1)	–	b.d.l.	b.d.l.	b.d.l.	b.d.l.			
Cr	0.02(1)	0.013(4)	0.02(1)	–	0.27(12)	0.26(2)	0.08(1)	0.11(1)			

Mn	0.03(1)	0.01(1)	0.01(1)	–	0.02(1)	0.11(1)	0.04(1)	0.07(1)
Se	0.45(3)	0.48(2)	0.47(4)	–	0.48(8)	0.53(8)	0.49(2)	0.52(3)
Te	0.18(5)	0.30(9)	0.43(17)	–	0.86(50)	0.27(13)	0.33(8)	0.21(5)
Pt	2.27(41)	0.18(16)	0.17(17)	–	–	8.37(131)	3.87(115)	5.56(162)
Total	96.58(26)	95.32(73)	95.59(77)	–	100.24(55)	100.75(35)	100.27(67)	100.77(35)
O (wt.%) <sup>calc</sup>	1.57	3.91	4.19	–	2.04	1.76	4.08	2.76
LA-ICP-MS	<i>N</i> = 4	<i>N</i> = 4	<i>n.a.</i>	<i>n.a.</i>	<i>n.a.</i>	<i>N</i> = 10	<i>N</i> = 4	<i>N</i> = 4
Pt (wt.%)	2.80(43)	0.49(6)	–	–	–	8.90(65)	6.73(165)	9.70(73)
Si (ppm)	496(91)	389(47)	–	–	–	550(76)	757(173)	1146(436)
Ca	653(125)	140(46)	–	–	–	736(132)	572(251)	802(307)
Ti	<i>Int.</i>	<i>Int.</i>	–	–	–	22(3)	63(16)	44(10)
V	9.9(7)	3.3(1)	–	–	–	4.6(4)	5.2(5)	5.4(2)
Cr	189(15)	98(7)	–	–	–	<i>Int.</i>	<i>Int.</i>	<i>Int.</i>
Mn	363(34)	125(11)	–	–	–	1099(48)	524(40)	768(15)
Co	29(3)	16(1)	–	–	–	19.2(5)	26(2)	24(1)
Ni	289(34)	168(14)	–	–	–	226(8)	268(31)	281(8)
Cu	402(27)	255(23)	–	–	–	457(22)	468(53)	603(19)
Zn	56(4)	64(5)	–	–	–	80(4)	46(3)	81(4)
Ga	1.70(8)	0.47(2)	–	–	–	0.82(7)	0.67(4)	0.78(13)
Ge	8.1(7)	6.6(6)	–	–	–	4.4(4)	9.0(10)	8.6(3)
As	39(5)	85(8)	–	–	–	31(4)	39(8)	44(8)
Se	3592(363)	2753(131)	–	–	–	4294(350)	4131(671)	5837(382)
Mo	155(16)	95(8)	–	–	–	86(2)	156(16)	132(1)
Sn	7.4(7)	20(1)	–	–	–	7.7(8)	21(5)	13(1)
Sb	14(1)	7.3(8)	–	–	–	1.61(10)	5.3(10)	2.8(2)
Te	2625(467)	2214(47)	–	–	–	2673(545)	3674(547)	5805(1236)
W	1.33(46)	0.13(2)	–	–	–	0.12(1)	0.11(4)	0.26(11)
Pb	8.7(2)	8.4(3)	–	–	–	3.8(8)	1.99(57)	5.0(12)

<sup>a</sup> Sulfide could not be analyzed as it was dispersed throughout the silicate melt as tiny specks only.

<sup>b</sup> *n.a.* = not analyzed.

<sup>c</sup> *N* = number of analyses.

<sup>d</sup> *b.d.l.* = below detection limit.

<sup>e</sup> Calculated O (wt.%) using the expression provided in [Kiseeva and Wood \(2015\)](#).

<sup>f</sup> Used as internal standard for LA-ICP-MS data processing.

determined sulfide-silicate partitioning behavior of these elements at high  $P$ - $T$ . Our experiments were also used to quantify the sulfide-silicate partitioning of siderophile elements V, Cr, Mn, Co, Cu, Zn, Ga, Ge, As, Se, Mo, Sn, Sb, Te, W and Pb. We studied to which extent their sulfide-silicate partitioning behavior may change with the various lunar melt compositions and redox conditions considered, and results are used to provide additional information about the possibility of sulfide saturation in the various lunar magma source regions.

## 2. METHODS

### 2.1. Experimental methods

High  $P$ - $T$  experiments were performed in a Bristol type end-loaded piston cylinder press (Boyd and England, 1960) in the high-pressure laboratory at the Vrije Universiteit Amsterdam, the Netherlands. Experiments were conducted in graphite capsules (1.7 mm O.D., 0.7 mm I.D., 4–5 mm long) that were placed in sealed Pt capsules (2 mm O.D., 1.7 mm I.D., 7–8 mm long). Two experiments were conducted in MgO capsules manufactured from high-purity crystalline MgO rods. Experiments were performed using synthetic silicate and sulfide mixtures. Silicates consisted of high-purity powdered oxides and carbonates representing synthetic analogues of the A14 black (A14BG) and yellow glass (A14YG), A15 green glass (A15GG), A17 orange glass (A17OG) and a late stage lunar magma ocean melt (LBS) (Tables 1 and 3). Silicate mixtures were first decarbonated by slowly heating the mixtures from 923 to 1273 K in a box furnace over a 7 h period. The mixtures were taken out of the oven, while the box furnace was heated to 1823 K. The mixtures were re-inserted in the furnace at 1823 K. After 15 min at 1823 K, the mixtures were rapidly quenched by immersing the bottom of the Pt crucible in water. With the exception of the A14YG composition, a glass shard of each of the starting compositions was kept for Electron Probe Microanalysis (EPMA) analysis (Table 1). Silicate starting compositions were always stored at 383 K in an oven to minimize atmospheric H<sub>2</sub>O contamination.

The sulfide powder mixture consisted of stoichiometric FeS plus 0.5 wt.% of Se and Te (all 99.5% purity; Alfa Aesar), thoroughly homogenized under ethanol in an agate mortar. The mixtures were then loaded into the capsules in a 2:1 to 3:1 silicate:sulfide ratio by volume. In the graphite capsule experiments, the silicate composition was sandwiched in between two FeS layers at the bottom and top of the capsule. This approach has previously proven to be successful to minimize significant Pt contamination of FeS liquids as the Pt will only concentrate in the upper blob placed adjacent to the lid of the graphite capsule bucket (Wykes et al., 2015). After insertion of the graphite capsules, Pt capsules were crimped and welded shut to prevent infiltration or loss of volatiles. This approach and the use of noble metal outer capsules have shown to result in < 500 ppm H<sub>2</sub>O contamination (Médard et al., 2008; Sarafian et al., 2017). The MgO capsules were closed with a tightly fitting MgO lid and were not contained within a noble

metal outer capsule. These runs may have experienced significantly more H<sub>2</sub>O contamination (see Section 3.5 and Vander Kaaden et al., 2015).

Experiments were performed at 1683–1883 K and 1–2.5 GPa using a 13 mm diameter talc-Pyrex pressure cell assembly that consists of concentric sleeves of natural talc (outer), Pyrex glass (inner), a graphite furnace and a MgO crushable spacer (Van Kan Parker et al., 2011) (Table 2). The pressure calibration of Van Kan Parker et al. (2011) was used which is based on the fayalite + quartz = ferrosillite and albite = jadeite + quartz equilibria, resulting in a friction correction of <3% and a pressure uncertainty of 0.1 GPa. Experimental run temperatures were measured and controlled using a type “D” W-Re (W<sub>97</sub>-Re<sub>3</sub> - W<sub>75</sub>-Re<sub>25</sub>) thermocouple contained in a four-bore alumina sleeve. A 0.6 mm thick ruby disc was used to prevent puncturing of the capsule by the thermocouple tip. The resulting increased distance between the thermocouple tip and sample results in a 10 K deviation from the measured temperature (Wood et al., 2014). Thermocouple temperatures were therefore set 10 K higher than the target sample temperature. Samples were heated at a rate of 100 K/min to 1073 K. At 1073 K, samples were sintered for 60 min to reduce surface tension and prevent exfiltration of sulfides into the capsule material. Samples were subsequently heated at a rate of 100 K/min to the desired peak temperatures while the pressure was gradually increased during heating. Run times (listed in Table 2) were between 0.5 and 2 h, depending on target temperature, to ensure a steady state between the sulfide and silicate (see Section 3.2). At the end of the desired run time, experiments were rapidly quenched by shutting off the power to the furnace while maintaining pressure. Capsules were mounted in petropoxy resin, sectioned perpendicular to the short capsule axis, and polished to a fine (<1 μm) finish using various grades of Al<sub>2</sub>O<sub>3</sub> polishing powder for subsequent microanalysis.

### 2.2. Analytical methods

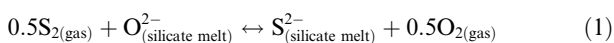
Experimental charges were analyzed for sulfide and silicate major element abundances with a JXA JEOL 8530F field emission electron probe microanalyser (EPMA) at the Dutch National Geological Facility at Utrecht University and with a JXA JEOL 8900 at the University of Münster, Germany (Tables 3 and 4). Sulfides and silicates were analyzed with a defocused beam, using a beam diameter (15 μm) that was roughly equivalent to the step size. Analyses were conducted using beam currents of 20 nA and an accelerating voltage of 15 kV. Counting times were 30 s for peak and 15 s for background for major elements (Si, Al, Ti, Cr, Mg, Fe, Mn, Ca), whereas counting times of 20 s peak and 10 s background was used for S. Sulfide standards were tephroite for Mn, chalcopyrite for S and pure metal standards for Cr, Fe and Pt. Silicate melt standards were diopside for Si and Ca, forsterite for Mg, corundum for Al, hematite for Fe, tephroite for Mn, KTiPO<sub>5</sub> for K, TiO<sub>2</sub> for Ti, jadeite for Na, chalcopyrite for S and pure metal standards for Se, Te, Cr and Pt.

Laser ablation inductively coupled plasma mass spectrometry (LA-ICP-MS) at University of Münster was used

to quantify the abundances of trace elements in the silicate melt ([Appendix Section A.1](#)). We used a 193 nm ArF excimer laser (Analyte G2, Photon Machines) with a repetition rate of 10 Hz and energy of  $\sim 3\text{--}4\text{ J/cm}^2$  throughout the entire session with beam sizes ranging between 25 and 50  $\mu\text{m}$ . We measured the following isotopes:  $^{29}\text{Si}$ ,  $^{43}\text{Ca}$ ,  $^{47}\text{Ti}$ ,  $^{48}\text{Ti}$ ,  $^{51}\text{V}$ ,  $^{53}\text{Cr}$ ,  $^{55}\text{Mn}$ ,  $^{59}\text{Co}$ ,  $^{60}\text{Ni}$ ,  $^{61}\text{Ni}$ ,  $^{63}\text{Cu}$ ,  $^{66}\text{Zn}$ ,  $^{69}\text{Ga}$ ,  $^{75}\text{As}$ ,  $^{82}\text{Se}$ ,  $^{95}\text{Mo}$ ,  $^{118}\text{Sn}$ ,  $^{121}\text{Sb}$ ,  $^{125}\text{Te}$ ,  $^{182}\text{W}$ ,  $^{195}\text{Pt}$  and  $^{208}\text{Pb}$ . The NIST 612 glass was used as an external reference material for both the metal and silicate. The Si abundances (silicates) and Cr, Mn or Ti abundances (sulfides) measured by electron microprobe were used as internal standards. USGS reference materials BIR-1G and BCR-2G were analyzed every  $\sim 20$  LA-ICP-MS spots to assess the analytical accuracy and precision of measured trace element concentrations in the silicate and sulfide melts. [Fig. S1](#) shows a comparison between measured and recommended trace element concentrations in silicate reference materials BIR-1G and BHVO-2G. We find good agreement between both values for the majority of the trace elements considered here, in agreement with our previous work ([Steenstra et al., 2017b,c](#)). We do note that  $^{63}\text{Cu}$  has a potential  $^{23}\text{Na}^{40}\text{Ar}$  interference during LA-ICP-MS analyses, which can yield an incorrect calibration when using the Na-rich NIST glasses. Fortunately, we find that there is also good agreement between measured concentrations of Cu in BIR-1G and BHVO-2G glasses, suggesting that measured Cu concentrations are not significantly affected by the  $^{23}\text{Na}^{40}\text{Ar}$  interference.

### 2.3. Thermodynamic background describing S solubility in silicate melts

The SCSS of a silicate melt varies with oxygen fugacity ( $f\text{O}_2$ ), sulfur fugacity ( $f\text{S}_2$ ), melt composition and  $P$ - $T$  ([O’Neil and Mavrogenes, 2002](#); [Wykes et al., 2015](#); [Smythe et al., 2017](#); [Ding et al., 2017](#)). Under reducing conditions, S dissolves in the silicate melt as  $\text{S}^{2-}$ , thereby replacing  $\text{O}^{2-}$  on the anion sublattice ([Fincham and Richardson, 1954](#)):



where the pseudo-equilibrium constant for the latter reaction is:

$$\ln(K_{(1)}) = \ln a_{\text{S}^{2-}}^{\text{silicate melt}} + 0.5 \ln f_{\text{O}_2}^{\text{gas}} - 0.5 \ln f_{\text{S}_2}^{\text{gas}} - \ln a_{\text{O}^{2-}}^{\text{silicate melt}} \quad (2)$$

The pseudo-equilibrium constant in Eq. (2) can be defined as the sulfur capacity or  $C_S$  ([O’Neil and Mavrogenes, 2002](#); [Ding et al., 2017](#)):

$$\ln C_S = \ln[\text{S}] + 0.5 \ln \frac{f_{\text{O}_2}}{f_{\text{S}_2}} \quad (3)$$

where  $[\text{S}]$  is the sulfur concentration in the silicate melt. Note that the term  $\ln a_{\text{O}^{2-}}^{\text{silicate melt}}$  from Eq. (2) can be ignored given that the abundance of  $\text{O}^{2-}$  ions greatly exceeds the abundance of  $\text{S}^{2-}$  ions in the silicate melt or  $a_{\text{O}^{2-}}^{\text{silicate melt}} \approx 1$  ([O’Neil and Mavrogenes, 2002](#)). The  $C_S$  can then be modeled as:

$$\ln C_S = A_0 + \sum_M X_M A_M \quad (4)$$

where  $X_M$  is the mole fraction of cation  $M$ , coefficient  $A_M$  represents the preference of cation  $M$  combining with S over O, and  $A_0$  is a constant ([O’Neil and Mavrogenes, 2002](#)). The first equation describes the silicate melt equilibrium with  $\text{S}_{2(\text{gas})}$ , whereas the SCSS represents the abundance of S in the silicate melt that is in equilibrium with a sulfide. The equilibrium between S in the silicate melt and liquid FeS is described by the following:



for which the equilibrium constant is ([Ding et al., 2017](#)):

$$\frac{-\Delta G^{(5)}}{RT} = \ln a_{\text{FeS}}^{\text{sulfide melt}} - \ln a_{\text{FeO}}^{\text{silicate melt}} + 0.5 \ln \frac{f_{\text{O}_2}}{f_{\text{S}_2}} \quad (6)$$

The combination of Eqs. (3) and (6) eliminates  $f\text{O}_2$  and  $f\text{S}_2$ , resulting in:

$$\ln[\text{S}]_{\text{SCSS}} = \frac{-\Delta G^{(5)}}{RT} + \ln a_{\text{FeS}}^{\text{sulfide melt}} - \ln a_{\text{FeO}}^{\text{silicate melt}} + \ln C_S \quad (7)$$

[Wykes et al. \(2015\)](#) expanded the latter model and included a pressure term:

$$\ln[\text{S}]_{\text{SCSS}} = \frac{-\Delta G^{(5)}}{RT} + \ln a_{\text{FeS}}^{\text{sulfide melt}} - \ln a_{\text{FeO}}^{\text{silicate melt}} + \ln C_S + \frac{CP}{T} \quad (8)$$

where  $C$  is a constant that describes the volume changes with variable pressures. [O’Neil and Mavrogenes \(2002\)](#) found an anomalous slope of  $\ln C_S$  with FeO in high-Ti basalts, relative to MORB-like basalts, and addressed this issue by addition of the empirical term of  $B_{\text{Fe-Ti}} X_{\text{Fe}} X_{\text{Ti}}$  to Eq. (4). As the focus of our study is predicting the SCSS for high-FeO lunar melt compositions, the term  $\ln a_{\text{FeO}}^{\text{silicate melt}}$  can be dropped as the negative effect of this term on the SCSS is relevant for silicate melt compositions containing  $< 5\text{ wt.}\%$  FeO only ([Wykes et al., 2015](#); [Ding et al., 2017](#)). This results in a parameterization of the SCSS with the following parameters:

$$\ln[\text{S}]_{\text{SCSS}}(\text{ppm}) = A + \frac{B}{T} + \sum C_i X_i + D X_{\text{Fe}} X_{\text{Ti}} + E \frac{P}{T} + \ln a_{\text{FeS}}^{\text{sulfide melt}} \quad (9)$$

where  $A$ ,  $B$ ,  $C_1$ ,  $C_2$ , ...,  $D$ ,  $E$  are regression constants,  $T$  is temperature in K,  $P$  is pressure in GPa and  $X_i$  represents the molar fraction of cation  $i$  in the silicate melt (i.e.  $X_{\text{Fe}}$ ,  $X_{\text{Ti}}$ ,  $X_{\text{Si}}$  ...).

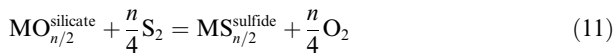
Sulfides in the lunar mantle may not be stoichiometric FeS (i.e.  $\ln a_{\text{FeS}}^{\text{sulfide melt}} \neq 1$ ). We therefore adopt a ternary symmetric solution approach as used by [Smythe et al. \(2017\)](#) to account for changes in SCSS due to deviations from pure FeS compositions and activities, in terms of addition of Ni and/or Cu:

$$\begin{aligned} \ln[\text{S}]_{\text{SCSS}}(\text{ppm}) = & A + \frac{B}{T} + \sum C_i X_i + D X_{\text{Fe}} X_{\text{Ti}} + E \frac{P}{T} \\ & + \ln X_{\text{FeS}}^{\text{sulfide}} + \frac{F}{T} (X_{\text{NiS}}^2 + X_{\text{NiS}} X_{\text{CuS}_{0.5}}) \\ & + \frac{G}{T} (X_{\text{CuS}_{0.5}}^2 + X_{\text{NiS}} X_{\text{CuS}_{0.5}}) \\ & + \frac{H}{T} (-X_{\text{NiS}} X_{\text{CuS}_{0.5}}) \end{aligned} \quad (10)$$

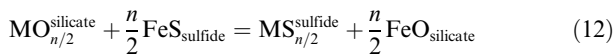
where parameters F, G and H are non-ideality parameters treated as unknowns. Parameter  $X_{\text{FeS}}^{\text{sulfide}}$ ,  $X_{\text{NiS}}$  and  $X_{\text{CuS}_{0.5}}$  are defined as  $\text{Fe}/(\text{Fe} + \text{Ni} + \text{Cu})$ ,  $\text{Ni}/(\text{Ni} + \text{Fe} + \text{Cu})$  and  $\text{Cu}/(\text{Cu} + \text{Fe} + \text{Ni})$  on a molar basis, respectively (Smythe et al., 2017).

#### 2.4. Systematics of sulfide-silicate partitioning of siderophile elements

The experiments were also used to study the sulfide-silicate partitioning of several volatile and refractory siderophile elements (V, Cr, Mn, Co, Cu, Zn, Ga, Ge, As, Se, Mo, Sn, Sb, Te, W and Pb). The sulfide-silicate partitioning of element  $M$  with valence  $n$  is controlled by the ratio of oxygen to sulfur fugacities (Kiseeva and Wood, 2015):



Kiseeva and Wood (2013) showed that chalcophile element partitioning can also be treated in terms of an exchange reaction between element  $M$  in the silicate melt and Fe in the sulfide liquid, removing the need to define  $f\text{O}_2$  and  $f\text{S}_2$ :



Sulfide-silicate partition coefficient  $D$  for element  $M$  can be defined as:

$$D_M^{\text{sulfide-silicate}} = \frac{C_M^{\text{sulfide}}}{C_M^{\text{silicate}}} \quad (13)$$

where  $C_M^{\text{sulfide}}$  and  $C_M^{\text{silicate}}$  are the weight concentration of element  $M$  in the sulfide silicate phase, respectively. Kiseeva

and Wood (2013) showed that the relationship between  $D$  and  $\text{FeO}$  in the silicate melt can be represented as:

$$D_M^{\text{sulfide-silicate}} \approx A + \frac{n}{2} \log[\text{FeO}_{\text{silicate}} (\text{wt.}\%)] \quad (14)$$

where  $A$  is a constant relative to the free energy of Fe- $M$  exchange. If element  $M$  behaves ideal, consideration of  $\log D$  versus  $\log \text{FeO}_{\text{silicate}}$  (wt.%) should therefore yield a slope which represents  $1/2$  of element  $M$  dominant valence state(s) in the silicate melt.

### 3. RESULTS

#### 3.1. Run products

Run products consisted of well segregated sulfide blobs in quenched silicate melts. A typical example is shown in Fig. 1. The majority of silicate melts quenched to a homogenous glass, while some silicate compositions, especially those that were run in MgO capsules, showed heterogeneous spinifex-type quench textures (Fig. 1; Table 3). In experiments at low  $T$  or high  $P$  olivine and/or opx formed in addition to silicate melt (Table 1). The mineral modes were usually < 30 per cent of the total silicate fraction, and in all cases crystal-free exposed surfaces of the quenched silicate melts could be analyzed using both EPMA and LA-ICP-MS (Table 1). EPMA analyses of silicate and sulfide phases are given in Tables 3 and 4. In all experiments that were conducted in MgO capsules, the FeS phases were dispersed in the silicate melt as small to tiny flecks and were not large enough to analyze with EPMA and/or LA-ICP-MS (Fig. 1). This wide-spread distribution of FeS specks is compatible with sulfide saturation of the silicate melt, which is confirmed by the comparable

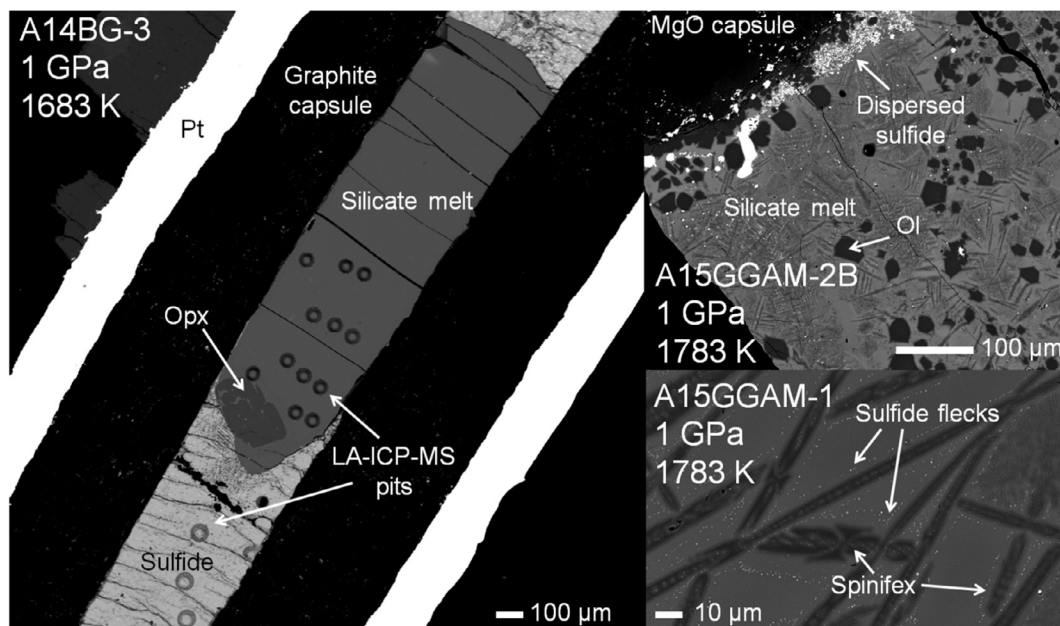


Fig. 1. Backscattered electron images of typical run products, showing the Pt or MgO outer capsule, graphite inner capsule and the variety of quench textures observed in the run products. See main text for details.

silicate S concentration in this experiment compared to experiments conducted at similar conditions. The absence of FeS specks does not imply that sulfide-silicate steady state was not attained (see next section) (Richter et al., 2009). The abundance and nature of FeS specks are dependent on the FeO content of the silicate melt (Wykes et al., 2015) as well as on the experimental  $P$ - $T$  conditions and the quenching rate (Boujibar et al., 2014). Care was taken to obtain “clean” EPMA measurements of the silicate melt and avoid larger ( $>10$   $\mu\text{m}$ ) dispersed sulfide blebs in the silicate melt. The smallest specks ( $<1$   $\mu\text{m}$ ) were included for determining the S content of the silicate melt, as they formed during quenching from high temperature at the end of the experiment (Boujibar et al., 2014). Due to small differences in sulfide-silicate powder mass ratios, FeO varied considerably between the experiments (Table 3). This also resulted in co-variation of other major element oxides.

### 3.2. Oxygen fugacity and activity of Fe in sulfides

The  $f\text{O}_2$  was calculated relative to the iron-wüstite buffer:

$$\begin{aligned} \Delta\text{IW} &= 2 \log \left( \frac{a_{\text{FeO}}^{\text{silicate}}}{a_{\text{Fe}}^{\text{sulfide}}} \right) \\ &= 2 \log \left( \frac{x_{\text{FeO}}^{\text{silicate}}}{x_{\text{Fe}}^{\text{sulfide}}} \right) + 2 \log \left( \frac{\gamma_{\text{FeO}}^{\text{silicate}}}{\gamma_{\text{Fe}}^{\text{sulfide}}} \right) \end{aligned} \quad (15)$$

where  $a_{\text{FeO}}^{\text{silicate}}$  and  $a_{\text{Fe}}^{\text{sulfide}}$  are the activities of FeO and Fe in the silicate and metallic melt,  $x_{\text{FeO}}^{\text{silicate}}$  and  $x_{\text{Fe}}^{\text{sulfide}}$  the molar fractions of FeO and Fe in the silicate and metallic melt, and  $\gamma_{\text{FeO}}^{\text{silicate}}$  and  $\gamma_{\text{Fe}}^{\text{sulfide}}$  their corresponding activity coefficients. Parameter  $\gamma_{\text{Fe}}^{\text{sulfide}}$  was calculated using the thermodynamic model of Lee and Morita (2002) (Appendix Section A.2). Parameter  $\gamma_{\text{FeO}}^{\text{silicate}}$  was considered to be ideal, given the unconstrained effects of Ti on  $\gamma_{\text{FeO}}^{\text{silicate}}$ . This approach yields  $\Delta\text{IW}$  values ranging between  $-2.7$  and  $-1.7$ . For comparison purposes, the  $\Delta\text{IW}$  values were also calculated assuming ideal  $\gamma_{\text{Fe}}^{\text{sulfide}}$ , which yield on average  $\sim 0.4$  to  $0.6$  higher  $\Delta\text{IW}$  (i.e. more oxidizing) (Table 2).

Due to the use of Pt outer capsules, some sulfides were contaminated with Pt. This is inherent to such experiments (Wykes et al., 2015). However, for the majority of the experiments the Pt concentration in the bottom blob is sufficiently low ( $<1.5$  wt.%) so that  $\gamma_{\text{Fe}}^{\text{sulfide}}$  will not be affected (Gudmundsson and Holloway, 1993; Kessel et al., 2001). Given the slightly different Pt contents of the lower and upper sulfide blobs, some gradient in S content may be expected in the silicate melt across the capsule due to the associated subtle changes in  $\gamma_{\text{Fe}}^{\text{sulfide}}$  (Wykes et al., 2015). All SCSS values reported in this work are based on data collected from the silicate melt closer to the bottom FeS-blobs that in most cases did not experience significant Pt-contamination (Wykes et al., 2015). Measurements were done at sufficient distance ( $>50$   $\mu\text{m}$ ) from the sulfide-silicate interface to prevent effects of secondary fluorescence of the sulfide on silicate melt measurements. In the case of run A17OG-7 where the bottom blob suffered significant Pt contamination ( $\sim 20$  wt.% Pt or  $x_{\text{Pt}}^{\text{sulfide}} = 0.06$ ), the

measured SCSS value should be considered as a lower limit. However, even for this degree of Pt contamination, the offset should be very limited according to thermodynamic data (Gudmundsson and Holloway, 1993; Kessel et al., 2001). The addition of up to 0.75 wt.% Se and 0.43 wt.% Te (usually less) will also not significantly change  $\gamma_{\text{Fe}}^{\text{sulfide}}$ . This is because their effects on  $\gamma_{\text{Fe}}^{\text{sulfide}}$  are likely to be similar as that for S on  $\gamma_{\text{Fe}}^{\text{sulfide}}$  given their overall similar geochemical behavior. Assuming their effects on  $\gamma_{\text{Fe}}^{\text{sulfide}}$  are similar, it would result in an increase of  $<0.01$  of  $\gamma_{\text{Fe}}^{\text{sulfide}}$  (Lee and Morita, 2002).

Note that some of the sulfides show low totals due to dissolved O (Kiseeva and Wood, 2013, 2015) which was not measured in this study (Table 4). This is particularly evident in the more FeO-rich runs, resulting in higher O contents in the metal. Addition of the concentrations of O calculated using the expression of Kiseeva and Wood (2015) yields sulfide totals that are close to 100%. Note that low totals in sulfides will not affect the outcome of this

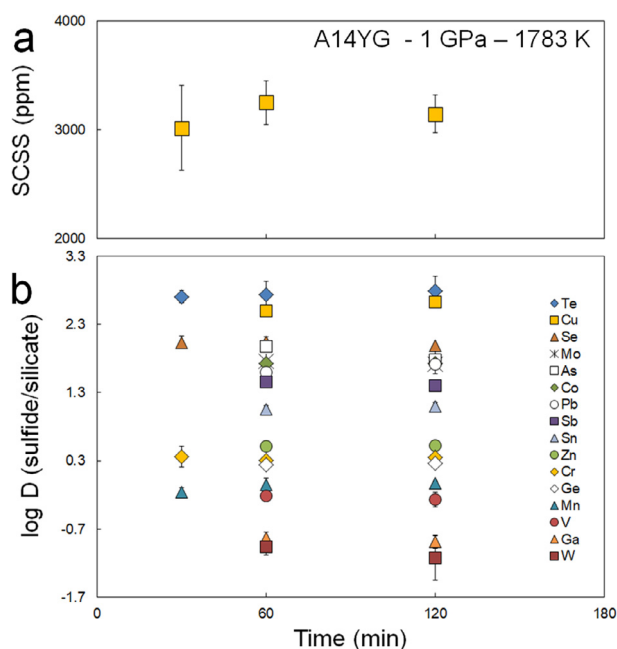


Fig. 2. Measured SCSS values and sulfide-silicate partition coefficients as a function of run time. (a) SCSS values of runs A14YG1-15A-C obtained at 1 GPa and 1783 K. After normalizing the SCSS values to a common molar Fe, Ti Si and Mg cation fraction ( $x_{\text{Fe}}^{\text{silicate}} = 0.16$ ;  $x_{\text{Ti}}^{\text{silicate}} = 0$ ;  $x_{\text{Si}}^{\text{silicate}} = 0.47$ ,  $x_{\text{Mg}}^{\text{silicate}} = 0.25$ ), using the dependencies from the SCSS parameterization that includes the sulfide compositional terms, the SCSS values are identical within error (Table 5). This suggests a steady-state between sulfide and silicate is attained within 30 min at 1783 K (see main text). (b) Sulfide-silicate partition coefficients of runs A14YG1-15A, A14YG1-15C and/or A14YG1-15B. All values were normalized to a common value of  $\Delta\text{IW} = -2$  according to their derived valence states (see Section 3.5). In case of Se and Te, their sulfide-silicate partition coefficients were normalized to  $x_{\text{FeO}}^{\text{silicate}} = 0.16$  using the dependencies of  $D_{\text{Se,Te}}$  reported in Steenstra et al. (2017b). After normalization, all values agree within error for each element, which confirms a steady-state is attained between sulfide and silicate melt within 30 min at 1783 K (see main text). The reader is referred to the online version of this paper for a colored version of this figure.

study, as these analyses are only provided to show that the silicate melts are in equilibrium with (close to) stoichiometric FeS. In addition, FeS-FeO melts exhibit only slight negative deviations from ideality (Nagamori and Yazawa, 2001), so that  $\gamma_{\text{Fe}}^{\text{sulfide}}$  will remain largely unaffected by the presence of O (Kiseeva and Wood, 2015).

### 3.3. Approach to a steady-state

Several lines of evidence can be used to argue that a steady-state between sulfide and silicate was approached in all experiments. We conducted a time series at 1783 K ranging between 30 and 120 min at peak temperatures (Table 2). After normalizing the SCSS data to a common silicate melt composition using the terms derived in this study (see Section 3.5), the SCSS values agree within error (Fig. 2a). In addition, the sulfide-silicate partition coefficients of all siderophile elements considered here do not vary within error with run time in these experiments (Fig. 2b). It is important to note that the diffusion coefficients for many of these elements (Cr, Mn, Ge) are several orders of magnitude lower than that for S at the same temperature (Zhang et al., 2010). This provides clear evidence that a steady-state is attained within <30 min at 1783 K, and most likely much faster. These observations are in good agreement with the results of Kiseeva and Wood (2013) who focused on sulfide-silicate partitioning of siderophile elements and report a steady state for sulfide-silicate within 30 min at 1683 K for many different (high-valence) elements.

In run products with Pt-free sulfides, the S concentrations at the lower and upper part of silicate melt were within error, whereas the Fe contents of the silicate melts are close or also within error. Slight variability can be attributed to the higher Pt contents of the top sulfide blobs (see previous sections). Additional evidence for the approach of a steady-state between sulfide and silicate in our experiments is provided by previous SCSS studies. For example, Liu et al. (2007) and Fortin et al. (2015) reported a sulfide-silicate steady-state to have occurred within 6 h at 1523 K and 1 GPa. Given the strong linear increase of diffusion coefficients with temperature (Zhang et al., 2010), the time required for a steady state of sulfide and silicate at >1683 K should be one or several orders of magnitude smaller than that observed at 1523 K. In addition, the reducing conditions in our experiments would result in far higher diffusion coefficients than reported by Zhang et al. (2010) for more oxidizing conditions. Approach of a steady state between sulfide and silicate within the reported run durations is also expected on the basis of the recent study of Smythe et al. (2017) that used similar (or shorter) run durations and found no evidence for the absence of a steady-state. However, it must be noted that Smythe et al. (2017) used pre-mixed silicate and sulfide powders, which is expected to result in more rapid achievement of a steady state between sulfide and silicate. Finally, the systematics found in this study (e.g. good reproducibility of  $P$ - $T$  effects on SCSS, valence states of siderophile elements) would not have been achieved if experiments did not attain a steady state between sulfide and silicate.

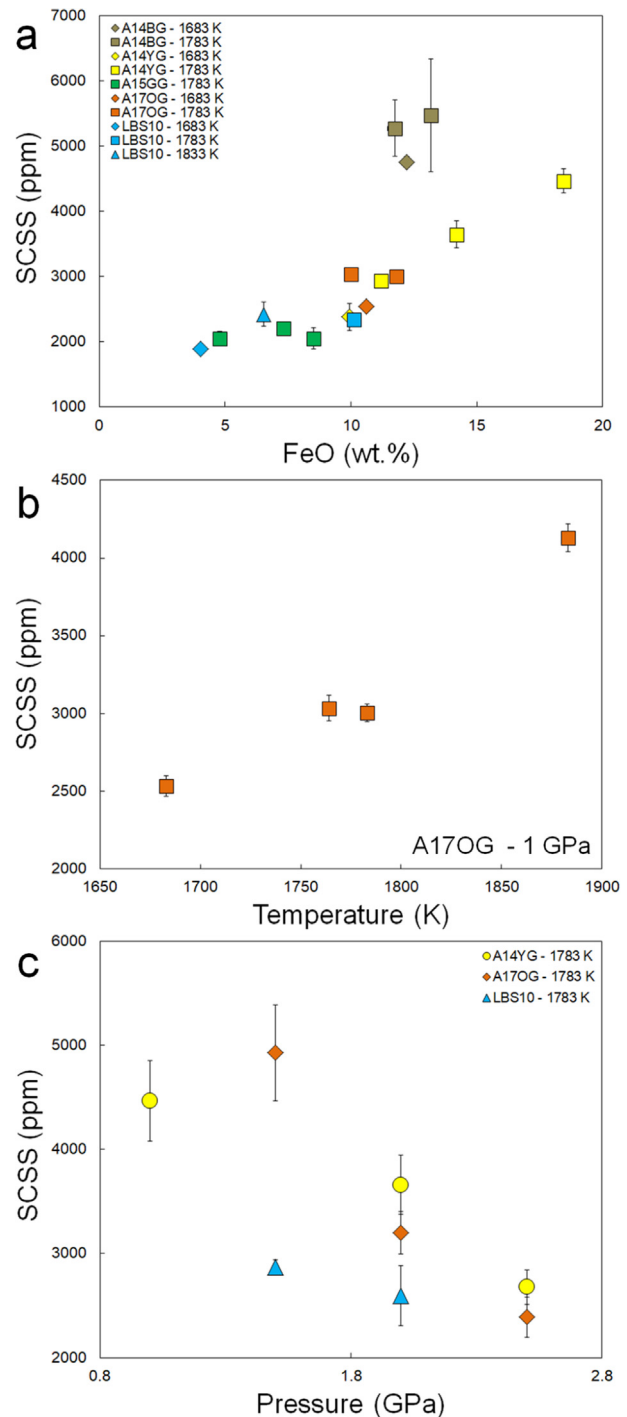


Fig. 3. SCSS values for lunar melts as a function of different variables. All errors are 2 SE (a) Uncorrected SCSS values obtained at 1 GPa and 1683–1833 K plotted versus FeO contents of the silicate melts. Errors are 2 SE and usually smaller than symbol size (b) Effects of temperature on the SCSS of the A17 orange glass (runs A17OG1 to 4). Experiments were performed at 1 GPa and experiments have similar FeO and TiO<sub>2</sub> contents (c) Effects of pressure on the SCSS of A14 yellow glass (runs A14YG1-15B, A14YG2-15, A14YG2.5-15), A17 orange glass (runs A17OG5 to 7) and of LBS10 (runs LBS1.5-15, LBS2-15) at 1783 K. All experiments within each series have similar FeO and TiO<sub>2</sub> contents. The reader is referred to the online version of this paper for a colored version of this figure.

### 3.4. Sulfur concentrations at sulfide saturation in lunar melts

Fig. 3a summarizes the SCSS values obtained in this study at 1 GPa and 1683–1833 K, plotted against  $\text{FeO}_{\text{silicate}}$ . Our results indicate that significant amounts of S can be dissolved in lunar melts, resulting in an overall SCSS range of 1900–7400 ppm, with the exact amount depending on temperature and/or composition. At first glance, the variation in SCSS at constant pressure is largely explained by differences in  $\text{FeO}_{\text{silicate}}$ . It is well established that silicate melt composition, including FeO, strongly affects SCSS (Ding et al., 2014; Wykes et al., 2015). However, a significant offset is observed between the most Ti-rich A14 black glass and the other compositions considered in this study. This suggests that besides  $\text{FeO}_{\text{silicate}}$ , other silicate melt compositional parameters may strongly affect the SCSS, as has been previously noted (O’Neil and Mavrogenes, 2002; Smythe et al., 2017; Ding et al., 2017). The effects of other silicate melt compositional parameters on the SCSS of lunar melts will be explored in Section 3.5.

Several experiments for each composition were performed at a constant pressure over a range of temperatures, yielding silicate melts that are similar in FeO and  $\text{TiO}_2$  contents. Fig. 3b shows the effects of  $T$  on the SCSS for the A17 orange glass composition. At constant pressure and near-constant melt composition, we find that the amount of S that can be dissolved in high-Ti lunar melts increases significantly with temperature. Between 1683 and 1883 K the SCSS increases by more than 1000 ppm. Similar increases of the SCSS as a function of temperature have been reported in previous studies (e.g., Liu et al., 2007; Ding et al., 2014, 2017; Smythe et al., 2017).

We also performed several pressure series to assess if pressure affects the SCSS for lunar magmas in the pressure range relevant to the Moon. Fig. 3c shows the result for the A14 yellow and A17 orange glass. For both series, a decrease of the SCSS with increasing pressure is observed at constant temperature. The SCSS decreases by 2000–2500 ppm in a 1.5 GPa pressure range. The decrease of the SCSS with pressure is in agreement with previous findings (e.g., Wendlandt, 1982; Mavrogenes and O’Neill, 1999; Ding et al. 2014, 2017; Smythe et al., 2017). The increase of the SCSS with temperature and decrease of SCSS with pressure agrees well with the outcome of the multi-linear regression analyses on compiled SCSS data (see Section 3.5).

### 3.5. New parameterizations for predicting SCSS of high FeO silicate melts

To predict the SCSS for the high FeO melts that characterize the Moon, we fit a combination of our data and previously published SCSS values for high FeO, nominally anhydrous melts only (>5 wt. FeO%) (Wendlandt, 1982; Mavrogenes and O’Neill, 1999; Li and Agee, 2001; Holzheid and Grove, 2002; O’Neil and Mavrogenes, 2002; Jugo et al., 2005; Liu et al., 2007; Brenan, 2008; Richter et al., 2009; Kiseeva and Wood, 2013; Ding et al., 2014; Fortin et al., 2015; Kiseeva and Wood, 2015; Wohlers and Wood, 2015; Wood and Kiseeva, 2015; Smythe et al., 2017; Ding et al., 2017;  $N = 337$ ; Supplementary Table 1)

to Eq. (10) using multi-linear regression. For experiments for which no O concentrations of the sulfides were reported, we use the model of Kiseeva and Wood (2015) to calculate the expected concentration of O in each of the sulfides. Note that we did not take the possible effect of O in the sulfide on SCSS explicitly into account. This should have no or very limited effects on the SCSS (Smythe et al., 2017). For comparison purposes, we also regressed all SCSS data without the use of such sulfide compositional terms (Table 5).

Table 5 lists the results of the regression. Our new parameterization that includes sulfide compositional terms reproduces the compiled dataset very well ( $R^2 = 0.95$ ; Table 5), predicting the increase of SCSS with temperature and decrease of SCSS with pressure (Table 5). Both the pressure and temperature are also in good agreement with regression results of previous workers. Ding et al. (2017) reported a  $1/T$  term of  $-4951(458)$  and a  $P/T$  term of  $-273(33)$ , which are statistically indistinguishable with the values reported here (Table 5). Similarly, Smythe et al. (2017) proposed an average  $P/T$  term of  $\sim -265(24)$  using various parameterization approaches. Their  $1/T$  term is, however, much larger than the one proposed here ( $\sim -14700$ ). This could be related to the incorporation of data from >5 GPa with corresponding higher temperatures in the latter dataset.

Fitting results without sulfide compositional terms show that sulfide composition is indeed an important parameter affecting the SCSS. Excluding sulfide composition terms results in a statistically non-significant  $P-T$  term and a much lower  $R^2$  given the similar number of fit parameters. Our new model confirms Cu and Ni in the sulfide decrease the SCSS of the coexisting silicate melt (Smythe et al., 2017). The effects of Ni and Cu in the sulfide on the SCSS are comparable, which implies that the SCSS decreases linearly with Fe content of the sulfide as previously observed (Smythe et al., 2017).

Table 5

Results of multi-linear regression of SCSS values of nominally anhydrous, high FeO (> 5 wt.%) silicate melts only ( $N = 337$ ; Supplementary Table 1) to Eq. (10). Regressions were performed by including sulfide composition terms (coefficients F, G and H) or excluding these terms. Numbers in parentheses represent 1 standard deviation in terms of last digits cited.

Term	Including sulfide composition terms Coefficient	Excluding sulfide composition terms Coefficient
A (constant)	14.69(32)	19.45(57)
B ( $1/T$ )	$-5020(319)$	$-7877(642)$
$CX_{\text{Si}}$	$-5.78(34)$	$-8.84(58)$
$CX_{\text{Ti}}$	n.s.s. <sup>a</sup>	5.71(277)
$CX_{\text{Al}}$	$-7.94(65)$	$-13.25(125)$
$CX_{\text{Fe}}$	2.15(40)	n.s.s.
$CX_{\text{Mg}}$	$-3.07(33)$	$-7.48(56)$
$CX_{\text{Ca}}$	n.s.s.	$-4.56(86)$
$DX_{\text{Fe}}X_{\text{Ti}}$	$-13.70(377)$	$-66.52(2031)$
E ( $P/T$ )	$-288(30)$	n.s.s.
F ( $X_{\text{NiS}}^2 + X_{\text{NiS}}X_{\text{CuS}_{0.5}}$ )	$-3759(245)$	–
G ( $X_{\text{CuS}_{0.5}}^2 + X_{\text{NiS}}X_{\text{CuS}_{0.5}}$ )	$-4047(110)$	–
H ( $-X_{\text{NiS}}X_{\text{CuS}_{0.5}}$ )	n.s.s.	–
$R^2$	0.95	0.71

<sup>a</sup> n.s.s. = not statistically significant.

Overall, we conclude that sulfide composition is an important parameter which should be included in parameterizations predicting SCSS for natural systems.

The effects of silicate melt composition derived here generally agree with previous results. Our results predicted the well-established increase of SCSS with  $X_{Fe}$ . We also find

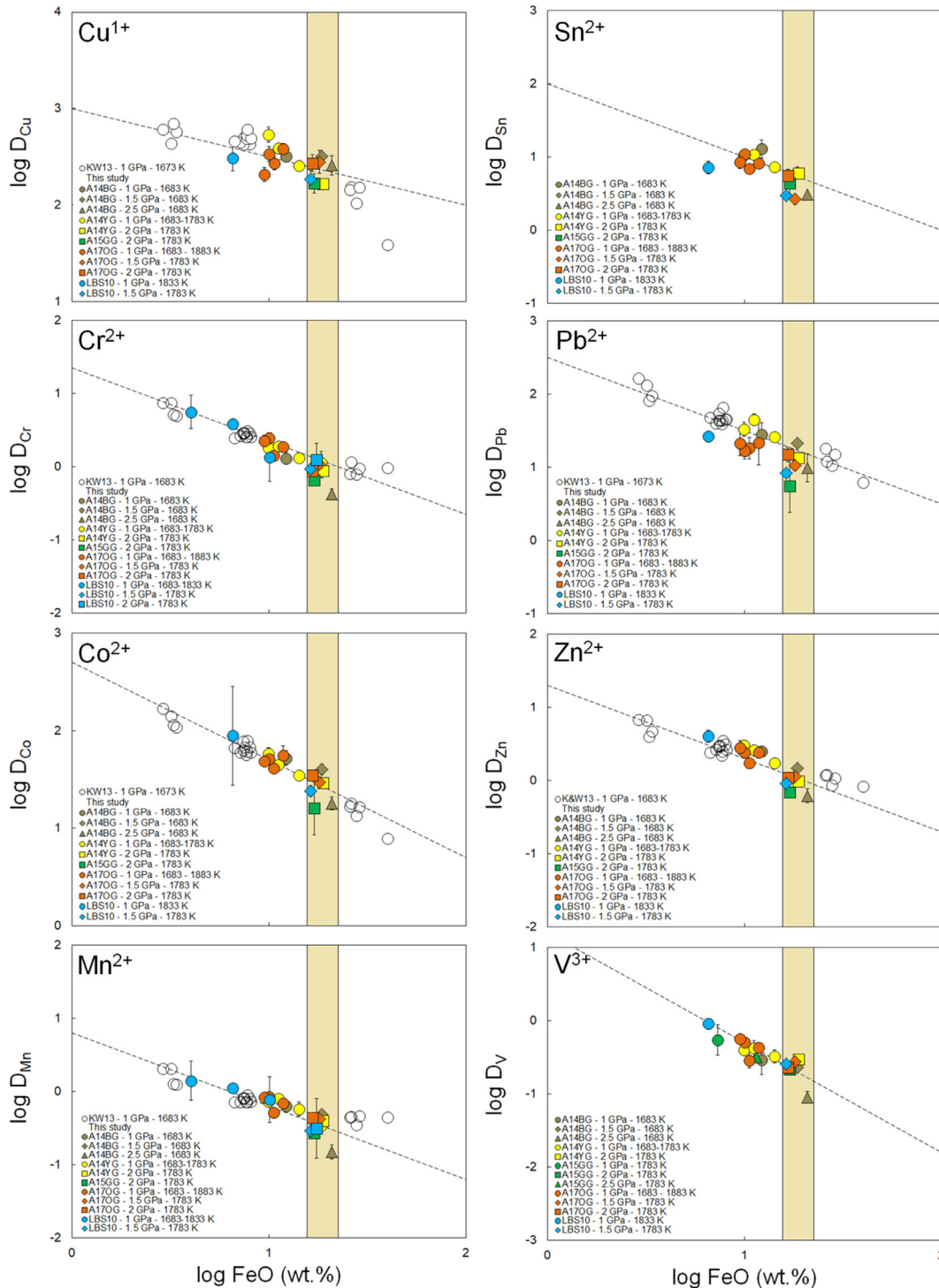


Fig. 4. Sulfide-silicate partition coefficients for low valence elements ( $D$ ) as a function of  $\log(\text{FeO}_{\text{wt.}\%})$ . Vertical shaded bar represents the estimated FeO range of primitive lunar glasses and mare basalts. Dashed line represents the slope corresponding with  $\frac{1}{2}$  of their valence (see Section 2.4). Plotted for comparison is sulfide-silicate partitioning data from Kiseeva and Wood (2013) obtained at 1 GPa and 1683 K (where available). All errors on  $D$  were calculated using simple error propagation and represents 2 SE for both EPMA and/or LA-ICP-MS measurements. (For interpretation of the references to colour in this figure legend, the reader is referred to the web version of this article.)

that the  $X_{Ti}$  term itself is not statistically significant, but that it indirectly results in a small decrease of the SCSS due to its lowering effects on the dependency of SCSS with

$X_{Fe_s}$  as proposed by O'Neil and Mavrogenes (2002). Our results also predict the decrease of SCSS with increasing silicate melt  $Al_2O_3$  and  $SiO_2$  content, as observed by O'Neil

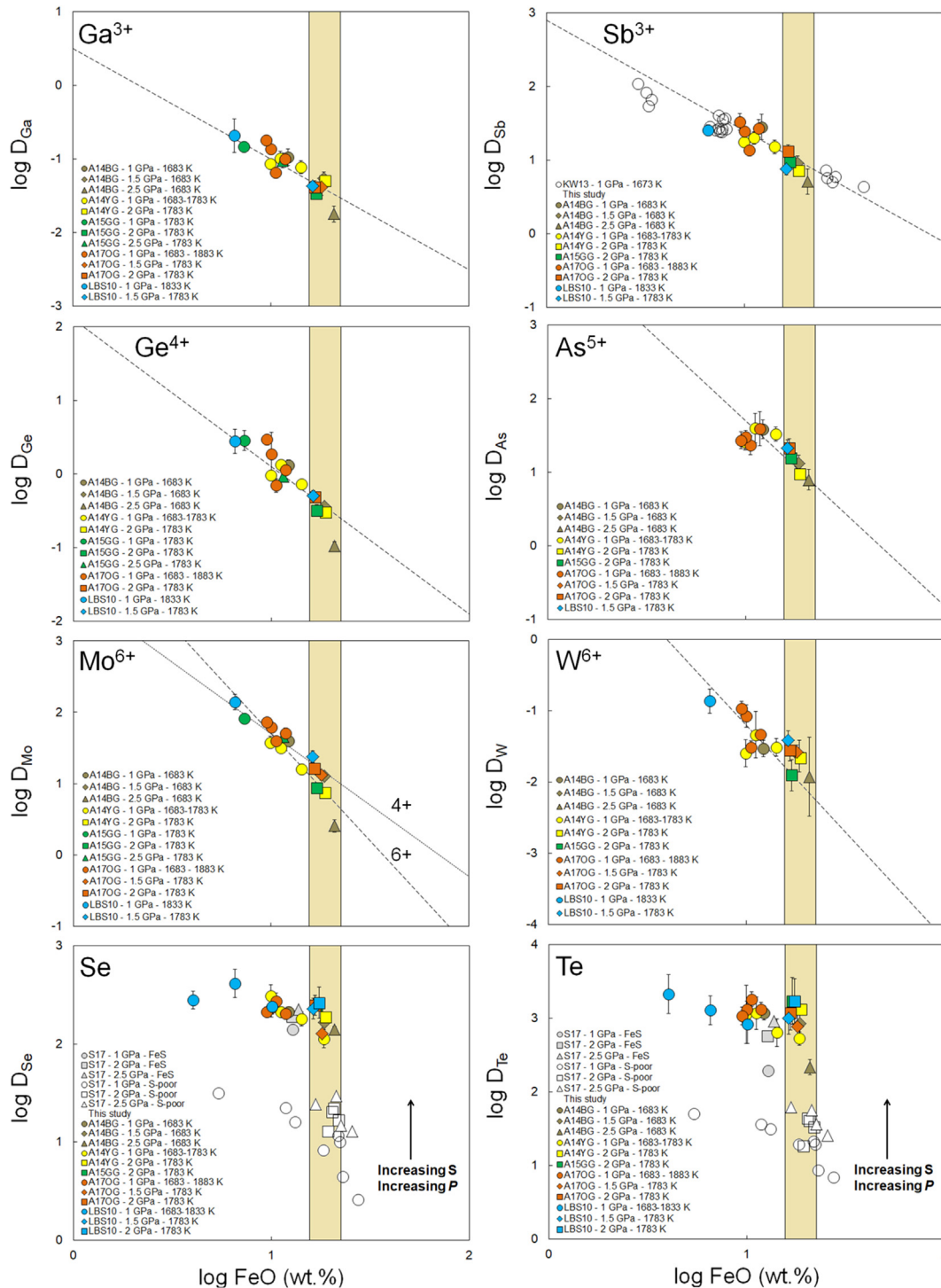


Fig. 5. Sulfide-silicate partition coefficients ( $D$ ) for low valence elements as a function of  $\log(\text{FeO}_{\text{wt.}\%})$ . Vertical shaded bar represents the estimated FeO range of primitive lunar glasses and mare basalts. Dashed line represents the slope corresponding with  $1/2$  of their valence (see Section 2.4). Plotted for comparison are sulfide-silicate partitioning data from Kiseeva and Wood (2013) obtained at 1 GPa and 1683 K (where available) and for  $Se$  and  $Te$  metal-silicate and sulfide-silicate partitioning data from Steenstra et al. (2017b). All errors on  $D$  were calculated using simple error propagation and represents 2 SE for both EPMA and/or LA-ICP-MS measurements. (For interpretation of the references to colour in this figure legend, the reader is referred to the web version of this article.)

and Mavrogenes (2002) for an anorthite-diopside eutectic composition.

Fig. 6 shows a comparison between measured and predicted SCSS values for high FeO (>5 wt.%) melts from this work and previous studies, using our new parameterization and the one recently reported by Ding et al. (2017). The thermodynamic approach used here to model the effects of Ni in sulfide on SCSS leads to a model that performs equally well as the empirical term from Ding et al. (2017) in terms of the effects of Ni in sulfide on the SCSS. Both models provide a satisfactory fit to currently available SCSS data. The parametrization reported by Ding et al. (2017) does not take the effect of Cu in sulfides into account. The significance of this parameter is clearly reflected by the large offset of SCSS data obtained for Cu-rich sulfide systems (Fig. 6). Our new model predicts the decrease of the SCSS with increasing Cu relatively well.

We also plotted our open-system (MgO-capsule) experiments for comparison purposes. These runs were not considered in the regression itself due to possible water contamination (e.g. Vander Kaaden et al., 2015). The SCSS values of low-Ti runs A15GGAM1 and 2B are in very good

agreement with the predicted SCSS values for these compositions (Fig. 6). However, the predicted SCSS values for high-Ti runs A14BGAM1 and 2 are much higher than the measured values. This does not reflect possible H<sub>2</sub>O contamination, which would result in an additional increase of the SCSS (Fortin et al., 2015). It likely reflects the breakdown of our model at very high (>20 wt.%) TiO<sub>2</sub> contents. We can also assess the effects of dissolved Pt by comparing the SCSS value of run A170G-7, where the sulfide suffered the most significant Pt contamination (20 wt.%), with the predicted SCSS value. The predicted value is slightly higher, but still falls within 50% uncertainty. This suggests that within the Pt range considered here, the SCSS is not significantly affected.

### 3.6. Sulfide-silicate partitioning of siderophile elements

Due to the use of FeS, Se and Te powders that were not of 100% purity (see Section 2.1), the experimental run products contained small but measurable amounts of several other elements besides Se and Te (V, Cr, Mn, Co, Cu, Zn, Ga, Ge, As, Mo, Sn, Sb, W and Pb). This enabled accu-

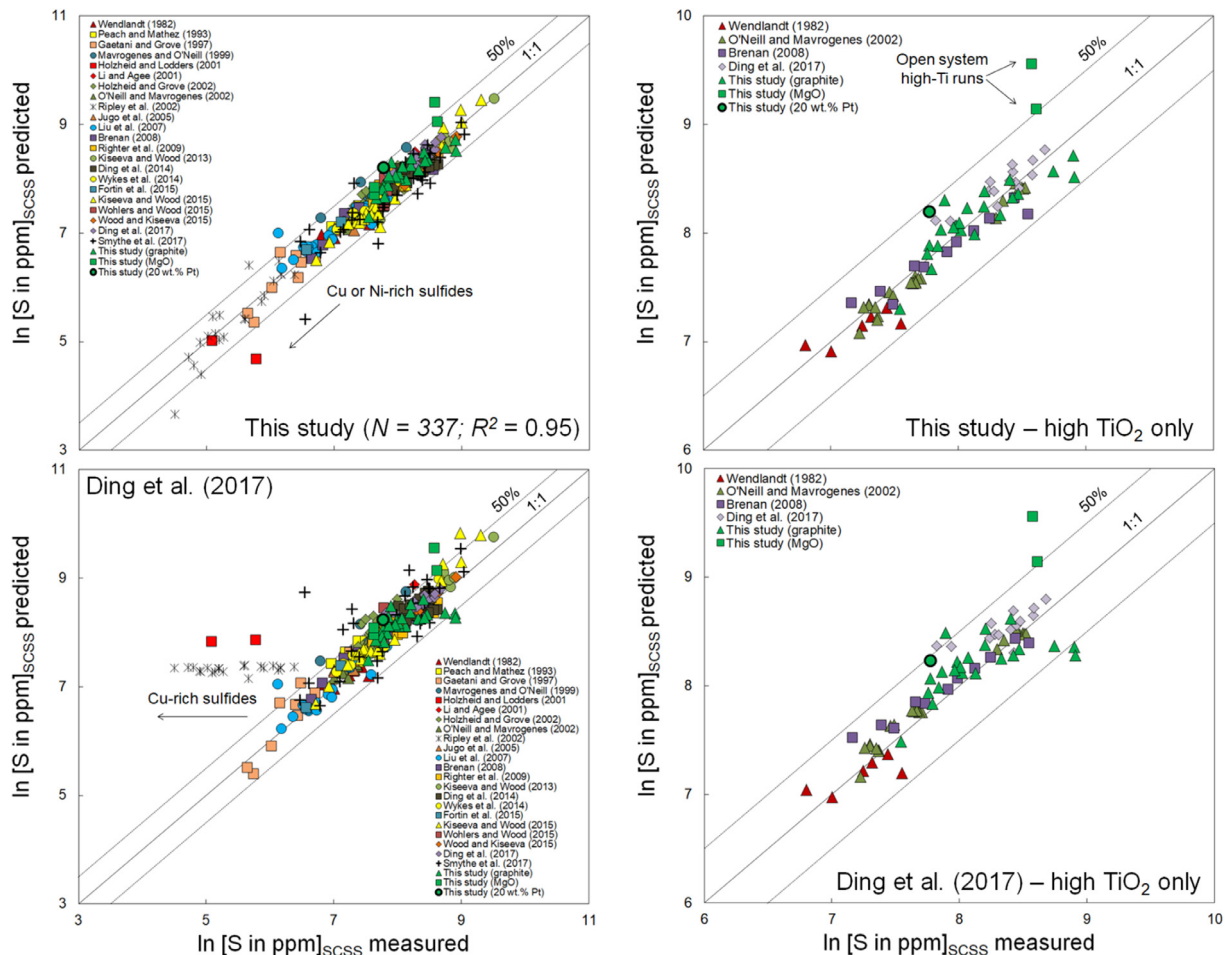


Fig. 6. Comparison between measured and predicted  $\ln[S \text{ in ppm}]_{\text{SCSS}}$  values using our new parameterization (Table 5; Eq. (10)) and that reported by Ding et al. (2017). Right panels show a comparison between measured and predicted  $\ln[S \text{ in ppm}]_{\text{SCSS}}$  for high-TiO<sub>2</sub> melts only. Solid line is a 1:1 identity line plotted for reference. Dashed lines represent 50% deviation from 1:1 identity line. (For interpretation of the references to colour in this figure legend, the reader is referred to the web version of this article.)

rate determination of their sulfide-silicate partitioning behavior in the majority of our experiments.

Figs. 4 and 5 show the measured sulfide-silicate partition coefficients. Our data suggests the following valence states: 1+ for Cu, 2+ for Cr, Mn, Co, Zn, Sn, Pb; 3+ for V, Ga, Sb; 4+ for Ge, 5+ for As, 4 or 6+ for Mo and 6+ for W. These findings are in good agreement with previous findings for metal-silicate systems (Corgne et al., 2008; Siebert et al., 2011; Righter et al., 2016) and sulfide-silicate systems (Kiseeva and Wood, 2013, 2015). It is possible that our suite of experiments shows the expected valence state transition from  $\text{Mo}^{6+}$  to  $\text{Mo}^{4+}$  at  $\sim\Delta IW = -1$  (Righter et al., 2016; Steenstra et al., 2017a,b,c), although this could also be a result of the effects of O on the activity of Mo in the sulfides. For Ge, the suggested 4+ valence state is marginally consistent with the observation that  $\text{Ge}^{2+}$  and  $\text{Ge}^{4+}$  exist in metal-silicate systems in roughly similar amounts at the redox conditions appropriate for our experiments, with the exact amount depending on metal and melt composition (Capobianco et al., 1999; Siebert et al., 2011). The slightly higher valence state could be related to the effects of dissolved O in the sulfide at high FeO contents. Kiseeva and Wood (2013, 2015) showed that with increasing  $\text{FeO}_{\text{silicate}}$  the O contents in sulfides increases, resulting in changes in the activities of some elements in the sulfides.

## 4. DISCUSSION

### 4.1. Sulfide saturation of lunar magma source regions?

Assessment of sulfide saturation in lunar melt source regions requires quantitative constraints on the major element and S abundances in these melts, as well as the inferred  $P$ - $T$  conditions at which these melts were generated. Table 6 lists the measured S abundances in the centers of volcanic glass beads and in whole-rock basalts (Delano et al., 1994; Meyer, 2011 and references therein; Hauri et al., 2015; Wing and Farquhar, 2015), and the experimentally determined multiple saturation points (MSP) for these compositions. The MSP provide one set of estimates for the conditions at lunar magma mantle sources.

The amount of S measured in a specific sample or sample group can then be compared with the predicted SCSS value for this composition. It is important to note that this approach only provides constraints on the presence or absence of sulfide saturation in the melt source region if the calculated SCSS represent the SCSS values of the melt in equilibrium with its mantle source.

We first focus on the most primitive lunar melts, namely the A12 and 15 low-Ti basalts and the volcanic picritic glass beads. These samples are likely to represent (near) primary melts (melt fraction  $F < 0.10$ ) from the lunar interior (e.g., Hughes et al., 1988, 1989; Shearer et al., 1991, 1996; Snyder et al., 1992; Beard et al., 1998; Table 6). As discussed in the study of Ding et al. (2017), there is some controversy about whether all of these melts are indeed primary magmas. Elkins et al. (2000) proposed that the A14B green glasses are products of fractional crystallization and assimilation of KREEP. However, Shearer et al. (1996) argued against assimilation of KREEP or ilmenite-rich cumulates on the

basis of Zr, Nb and Ce systematics in the lunar volcanic glasses.

Given the primitive nature of the low-Ti basalts and the volcanic lunar glasses, the measured and reconstructed amounts of S in these samples can be directly compared with the calculated SCSS values for these compositions. Fig. 7 shows the predicted SCSS values for each of these compositions and the measured S abundances for these samples or sample groups from previous studies (Table 6). For a pure FeS phase, calculated SCSS values are all at least 1500 ppm higher than the measured values within these samples.

Sulfides in the lunar mantle may not be stoichiometric FeS. Assuming end member values of 20 wt.% Ni or 20 wt.% Cu in the sulfides lowers SCSS values significantly, but in all cases they are still significantly higher than measured S abundances. We note that the reconstructed S abundances, corrected for the maximum extent of inferred degassing of S from samples during their eruption at the lunar surface, are also significantly lower than calculated SCSS values, independent of sulfide composition. This will be discussed in more detail in Section 4.2.

The  $P$ - $T$  conditions at the MSP used for the calculations presented above do not necessarily represent the  $P$ - $T$  conditions at which the magma is in equilibrium with the mantle source. As melt compositions represent aggregated liquids from polybaric near-fractional melting, the MSP likely reflects the average  $P$ - $T$  conditions of extraction of incremental liquids (Elkins-Tanton et al., 2003; Asimow and Longhi, 2004). Such uncertainties are not likely to affect the outcome of this study, as we will later show that the differences between calculated SCSS values and measured S contents are much larger than the expected effects from uncertainties in the  $P$ - $T$  conditions of the MSP for each melt.

Unlike the low-Ti basalts and the picritic glass beads, the lunar high-Ti basalts have undergone extensive fractionation, which could have resulted in an increase of S if S behaves as an incompatible element. The decrease in melt MgO content as a function of fractional crystallization should also be taken into account, as this affects the calculated SCSS value (Table 5).

To our knowledge, as of yet no high-pressure liquid lines of descent for high-Ti lunar melt compositions have been reported in the literature. We therefore computed the SCSS along the liquid line of descent at 1 bar, as determined experimentally for A17 high-Ti basalt 70017 (Rutherford et al., 1974). Fig. 8 shows the SCSS values that were calculated along this liquid line of descent for different sulfide compositions, assuming the  $P$ - $T$  conditions inferred for the MSP of these basalts (Fig. 8a) or the proposed  $T$  curve along the liquid line of descent at 1 atm (Fig. 8b). We find that the measured S contents in A17 high-Ti basalts are in all cases lower than the predicted range of SCSS values for a pure FeS phase, except for the most evolved compositions. The SCSS values do overlap when sulfides with 20 wt.% Ni or Cu are considered. As previously stated, the liquid line of descent for A17 basalt 70017 was determined at 1 atm and corresponding low temperature. Real melting temperatures and pressures were likely higher (Table 6),

Table 6  
Measured concentrations of S in high Ti lunar magmas and inferred  $P$ - $T$  conditions for their formation.

	P (GPa)	T (K)	$F$ (%) <sup>a</sup>	SiO <sub>2</sub> (wt.%)	TiO <sub>2</sub>	Al <sub>2</sub> O <sub>3</sub>	FeO	MgO	CaO	S (ppm)	S corr. for degassing <sup>b</sup>	S corr. for FC <sup>c</sup>	SCSS Pure FeS	FeS + 20% Cu	FeS + 20% Ni
<i>Basalts</i>											10%				
A11 high-Ti	0.85 ± 0.25 <sup>d</sup>	1495 ± 10 <sup>d</sup>	50–60 <sup>e</sup>	40.8 ± 1.1 <sup>[1]</sup>	11.2 ± 0.8	9.4 ± 1.2	18.9 ± 0.7	7.3 ± 0.8	11.2 ± 0.8	1940 ± 340 <sup>[1,2]</sup>	2156 ± 378	–	–	–	–
A12 low-Ti	1.5 ± 1.0 <sup>[3,4]</sup>	1700 ± 75 <sup>[5]</sup>	7–10 <sup>[4]</sup>	44.9 ± 1.6 <sup>[1]</sup>	3.5 ± 0.9	9.2 ± 1.7	20.5 ± 1.4	10.8 ± 3.8	9.8 ± 1.6	741 ± 207 <sup>[1,2]</sup>	823 ± 230 <sup>i</sup>	74 ± 32	3525 ± 1101	2510 ± 784	2452 ± 766
A15 low-Ti	1.5 ± 1.0 <sup>f</sup>	1700 ± 75 <sup>f</sup>	3 <sup>[6]</sup>	47.0 ± 1.6 <sup>[1]</sup>	2.0 ± 0.4	9.1 ± 0.6	20.7 ± 1.2	9.3 ± 1.0	10.4 ± 0.6	628 ± 125 <sup>[1,2]</sup>	698 ± 139	21 ± 4	3395 ± 1060	2418 ± 755	2362 ± 737
A17 high-Ti	0.85 ± 0.25 <sup>[7,8]</sup>	1495 ± 10 <sup>[7,8]</sup>	50–60 <sup>[9,10]</sup>	39.0 ± 1.2 <sup>[1]</sup>	12.1 ± 1.1	9.0 ± 0.7	18.9 ± 0.7	8.4 ± 1.2	10.8 ± 0.7	1600 ± 210 <sup>[1,2]</sup>	1778 ± 233	–	–	–	–
<i>Picritic glasses</i>											63% <sup>g</sup>				
A12 red	2.4 <sup>[11]</sup>	1730 <sup>[11]</sup>	4–7 <sup>g</sup>	33.4 <sup>[12]</sup>	16.4	4.6	23.9	13.0	6.3	376 ± 91 <sup>[13]</sup>	1016 ± 246	60 ± 29	5281	3761	3674
A14 black	1.5 <sup>[14]</sup>	1700 <sup>[14]</sup>	4–7 <sup>g</sup>	34.0 <sup>[15]</sup>	16.4	4.6	24.5	13.3	6.9	536 ± 103 <sup>[13]</sup>	1449 ± 278	84 ± 37	5957	4242	4143
A14B green	2.4 <sup>[16]</sup>	1833 <sup>[16]</sup>	4–7 <sup>g</sup>	44.8 <sup>[15]</sup>	0.45	7.1	19.8	19.1	8.0	265 ± 46 <sup>[13]</sup>	716 ± 124	41 ± 18	3745	2667	2605
A15A green	2.2 <sup>[17]</sup>	1793 <sup>[17]</sup>	4–7 <sup>[6]</sup>	45.7 ± 0.2 <sup>[18]</sup>	0.38 ± 0.03	7.5 ± 0.1	20.1 ± 0.2	17.3 ± 0.1	8.5 ± 0.1	116 ± 31 <sup>[18]</sup>	313 ± 84	19 ± 9	3569	2542	2483
A15B green	1.8 ± 0.5 <sup>[17]</sup>	1793 <sup>[17]</sup>	4–7 <sup>[6]</sup>	47.2 ± 1.0 <sup>[18]</sup>	0.42 ± 0.10	8.3 ± 1.3	18.4 ± 0.8	16.8 ± 1.7	8.2 ± 1.0	196 ± 48 <sup>[18]</sup>	529 ± 129	31 ± 15	3568 ± 265	2345 ± 189	2290 ± 184
A15C green	1.2 ± 0.6 <sup>[17]</sup>	1793 <sup>[17]</sup>	4–7 <sup>[6]</sup>	48.2 ± 0.2 <sup>[18]</sup>	0.23 ± 0.01	7.4 ± 0.1	16.8 ± 0.1	18.3 ± 0.2	8.4 ± 0.1	230 ± 7 <sup>[18]</sup>	621 ± 20	35 ± 10	3424 ± 331	2439 ± 235	2382 ± 230
A15D green	2.2 <sup>h</sup>	1793 <sup>h</sup>	4–7 <sup>[6]</sup>	45.3 ± 0.2 <sup>[18]</sup>	0.40 ± 0.02	7.2 ± 0.1	20.7 ± 0.2	17.7 ± 0.3	8.2 ± 0.1	111 ± 26 <sup>[18]</sup>	300 ± 71	18 ± 8	3698	2633	2572
A15E green	2.2 <sup>h</sup>	1793 <sup>h</sup>	4–7 <sup>[6]</sup>	45.3 ± 0.1 <sup>[18]</sup>	0.42 ± 0.02	7.1 ± 0.1	20.5 ± 0.2	18.2 ± 0.1	8.0 ± 0.1	137 ± 39 <sup>[18]</sup>	371 ± 106	22 ± 11	3658	2605	2544
A15A red	2.4 <sup>[11]</sup>	1730 <sup>[11]</sup>	4–7 <sup>g</sup>	35.6 ± 1.0 <sup>[18]</sup>	13.8	7.2 ± 0.1	21.9 ± 0.1	12.1 ± 0.1	7.9 ± 0.1	484 ± 35 <sup>[13]</sup>	1308 ± 95	74 ± 25	4531	3227	3152
A15 yellow	2.7 ± 0.3 <sup>i</sup>	1825 ± 25 <sup>i</sup>	4–7 <sup>g</sup>	42.9 ± 0.1 <sup>[18]</sup>	3.5 ± 0.2	8.2 ± 0.2	22.4 ± 0.2	13.3 ± 0.5	8.3 ± 0.2	414 ± 126 <sup>[13,18]</sup>	1211 ± 251	71 ± 32	4065 ± 369	2895 ± 263	2827 ± 257
A17 orange	2.8 ± 0.3 <sup>[19,20]</sup>	1825 ± 25 <sup>[19,20]</sup>	4–7 <sup>[21]</sup>	39.0 ± 0.3 <sup>[18]</sup>	9.3 ± 0.4	5.6 ± 0.3	22.4 ± 0.2	14.5 ± 1.1	7.4 ± 0.4	300 ± 116 <sup>[13,18]</sup>	814 ± 314	49 ± 29	4753 ± 433	3385 ± 308	3306 ± 301

<sup>a</sup> Degree of melting.

<sup>b</sup> S contents corrected for degassing assuming 10% of degassing for lunar mare basalts (Wing and Farquhar, 2015) and 63% for lunar volcanic glasses (Hauri et al., 2015).

<sup>c</sup> S contents corrected for degree of melting (i.e. mantle source contents), assuming S behaves like a highly incompatible element ( $D = 0.001$ ). Contents were calculated using the relationship

$\frac{C_S^L}{C_S^0} = F^{(D-1)}$ , where  $C_S^L$  and  $C_S^0$  represent the concentrations of S in the liquid and in the initial system,  $F$  is degree of melting and  $D$  is the partition coefficient, while assuming the estimated degrees of melting for each composition listed in the table.

<sup>d</sup> Based on estimates for A17 high-Ti basalts.

<sup>e</sup> Based on estimated  $F$  range of A17 high-Ti basalts. Average % degassing inferred for Apollo 17 orange glass beads (Hauri et al., 2015).

<sup>f</sup> Based on estimates for A12 low-Ti basalts (Papike et al., 1976; Walker et al., 1976b).

<sup>g</sup> Based on estimate for A17 orange glass (Hughes et al., 1989).

<sup>h</sup> Based on estimate for A15A green glass (Elkins-Tanton et al., 2003).

<sup>i</sup> Based on estimate for A12 yellow glass (Beard et al., 1998).

<sup>j</sup> Note that this value is within error with the value of 1050 ppm S proposed by Bombardieri et al. (2005) based on melt inclusions in A12 low-Ti basalts.

[1] Lunar Sample Compendium (Meyer, 2011).

[2] Wing and Farquhar (2015); *whole rock*.

[3] Papike et al. (1976).

[4] Bombardieri et al. (2005).

[5] Walker et al. (1976b).

[6] Hughes et al. (1988).

[7] Green et al. (1975).

[8] Longhi (1974).

[9] Neal et al. (1990).

[10] Neal et al. (1992).

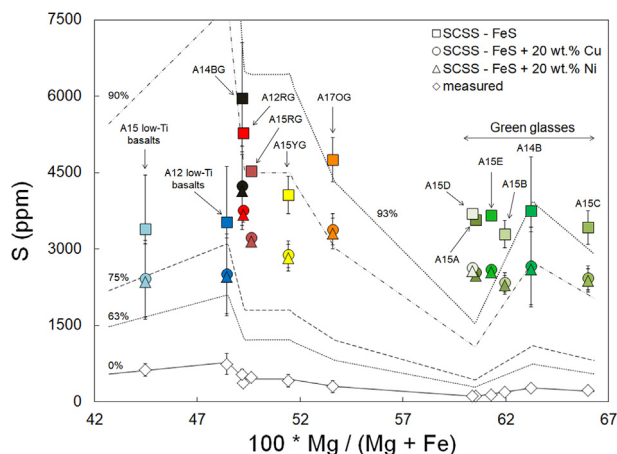


Fig. 7. Comparison between measured S abundances in primitive ( $F < 0.10$ ) lunar melts (open diamonds) and predicted SCSS values (filled symbols). Squares represent the SCSS values calculated for a pure FeS phase, filled circles for FeS + 20 wt.% Cu and filled triangles for FeS + 20 wt.% Ni. Sources of major and minor element compositions are reported in Table 6. Lines represent different degrees of degassing of S (0, 63, 75, 90 and 93%, respectively). Errors are maximum errors. For other details, see main text. (For interpretation of the references to colour in this figure legend, the reader is referred to the web version of this article.)

which would increase the SCSS (Fig. 8a). In the latter case, virtually all samples have S contents that fall below the SCSS range calculated for stoichiometric FeS.

#### 4.2. Constraints on the extent of sulfur degassing from lunar magmas

One possible explanation for the significantly lower S abundances in lunar low- and high-Ti melts, relative to the inferred SCSS values for these melts, is degassing of S. A recent study of Wing and Farquhar (2015) provided analyses of S abundances in low- and high-Ti lunar basalts and corresponding S isotopic compositions. They found that the low- and high-Ti lunar basalts show a very uniform  $\delta^{34}\text{S}$  value, suggesting  $< 10\%$  degassing of S from these basalts during or after eruption (Wing and Farquhar, 2015).

Assuming 10% degassing for the average S abundances in Apollo 12 and 15 low-Ti basalts yields S abundances that are still  $> 700$  ppm lower than any of the SCSS values calculated in this study (Fig. 7, Table 6). The difference is significantly increased when a pure FeS phase is considered (Fig. 7). For the A17 high-Ti lunar basalts, some corrected values overlap with the SCSS field for pure FeS, but only for the most evolved samples (Fig. 8). In general, most values are still lower than the required SCSS range for pure FeS.

In the case of the volcanic glasses, significantly higher degrees of degassing of S (and other chalcophile elements; e.g., Renggli et al., 2017) are expected due to the different eruption style (fire-fountaining) and as inferred from the volatile-rich coating on these glass beads (e.g., Delano

- [11] Delano et al. (1980).  
 [12] Marvin and Walker (1978).  
 [13] Delano et al. (1994); *center of volcanic glass beads*.  
 [14] Wagner and Grove (1997).  
 [15] Delano (1986a).  
 [16] Elkins et al. (2000).  
 [17] Elkins-Tanton et al. (2003).  
 [18] Hauri et al. (2015); *center of volcanic glass beads*.  
 [19] Krawczynski and Grove (2008).  
 [20] van Kan Parker et al. (2011a,b).  
 [21] Hughes et al. (1989).

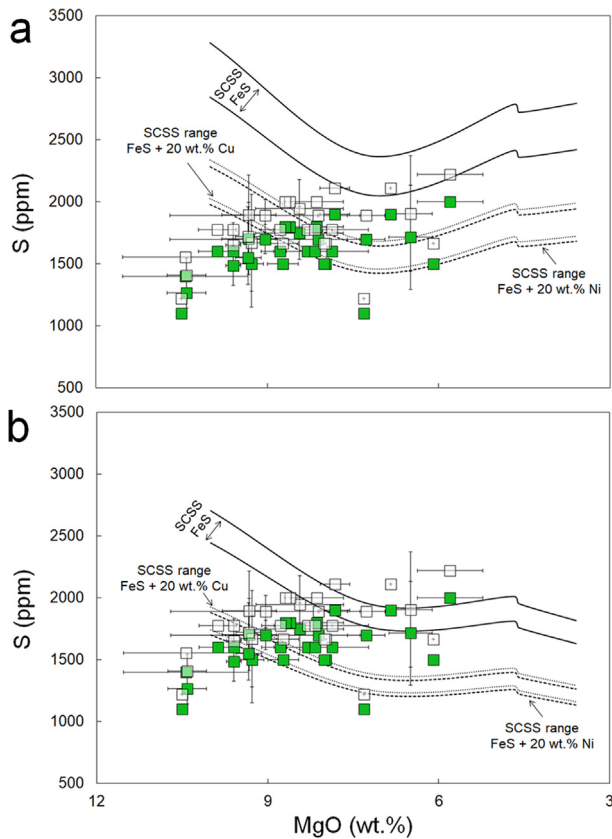


Fig. 8. Comparison between measured S abundances in A17 high-Ti lunar basalts (filled squares) and corrected S abundances assuming 10% degassing of S (open squares) with the calculated SCSS values based on silicate melt compositional evolution along the liquid line of descent reported for A17 high-Ti basalt 70017 (Rutherford et al., 1974). The SCSS values were calculated assuming (a) the  $P$ - $T$  conditions range of the MSP point proposed for the A17 high-Ti basalt suite (Table 6) and (b) using the  $T$  determined along the liquid line of descent determined for A17 high-Ti basalt 70017 at 1 atm (Rutherford et al., 1974).

et al., 1994; Hauri et al., 2015). Hauri et al. (2015) estimated the pre-eruptive abundance of volatile elements in the orange volcanic glass by adding the measured surface coating to the degassed composition, while assuming the S abundance in the least degassed melt inclusion in the Apollo 17 orange glass (74220, 884 ppm S) to be the initial value. This approach suggests that 63% of the initial S (corresponding to  $\sim 560$  ppm) degassed during eruption. Assuming a similar extent of degassing for the other low and high-Ti volcanic glass beads implies that the indigenous S abundances in volcanic glasses are still  $> 1200$  ppm lower than the SCSS values for these compositions (Fig. 7). These differences increase to over 2000 ppm if a pure FeS phase is considered. Reconstructed S abundances are close to the calculated SCSS values for a pure FeS phase only at degassing percentages exceeding  $> 90\%$ .

Although extensive degassing of S may occur when the melt droplets are in a liquid state, both the radiative cooling rate of such droplets in a vacuum (1100 K/sec) and the critical cooling rates of lunar picritic materials are very high

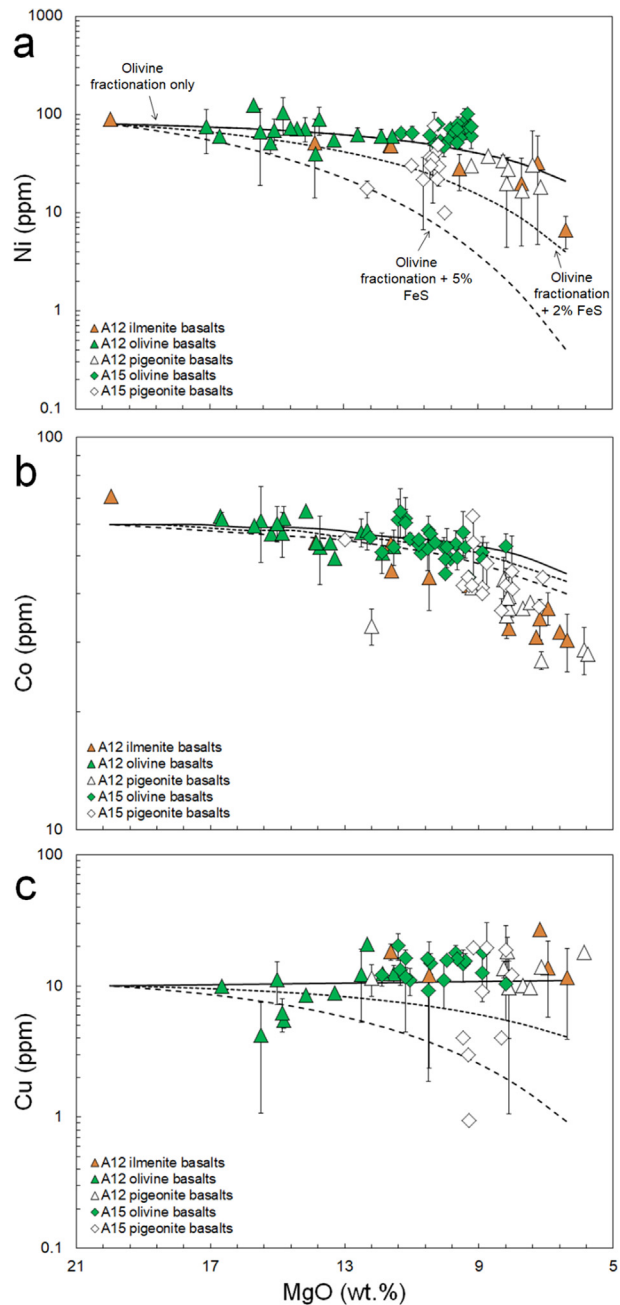


Fig. 9. Comparison between measured abundances of Ni (a), Co (b) and Cu (c) in Apollo 12 and 15 low-Ti basalts as a function of MgO (in wt.%) and modeled 10% Rayleigh fractionation lines involving olivine fractionation only (solid lines), olivine + 2% stoichiometric FeS (fine dashed lines) and olivine + 5% stoichiometric FeS (coarse dashed lines). Major and element compositions of the various lunar basalts were taken from Meyer (2011) and references therein. Vertical errors represent 1 standard deviation. Details on the modeling of the olivine-silicate melt and sulfide-silicate melt partitioning behavior of Ni, Co, Cu is provided in Section 4.3. (For interpretation of the references to colour in this figure legend, the reader is referred to the web version of this article.)

(1–100 K/sec) (Arndt and von Engelhardt, 1987; Delano et al., 1994). Retardation in cooling likely occurred due to a hot vapor environment and/or radiation shielding effects

in a dense cloud of radiating droplets (Arndt and von Engelhardt, 1987). However, it seems unlikely that there is sufficient time to degas the amount of S that is required to move S contents in these melts down from the SCSS value to the abundances measured in the sample. Saal et al. (2008) considered a scenario of slow cooling rates and found that the Apollo 15 low-Ti green glass only experienced 19% loss of S during a 300 s interval of diffusive volatile loss. More extensive degassing of S is excluded by the relatively low S content of melt inclusions within these beads, compared to rim values.

Finally, we note that it is now well established that lunar basalts and volcanic glasses were not completely anhydrous upon eruption (e.g., Saal et al., 2008; Hauri et al., 2011, 2015; Tartèse et al., 2013). All SCSS calculations used here assume anhydrous conditions, given the uncertainties in initial abundances of hydrogen in these melts. The addition of hydrogen will result in slightly higher SCSS values (e.g., Fortin et al., 2015), which implies that the SCSS values reported here are likely underestimates – the presence of any hydrogen in the Moon during formation of high-FeO magmas would make sulfide saturation in the source regions of these melts even more unlikely. For example, assuming 4 to 7% batch melting of a lunar source region that contains 100–300 ppm H<sub>2</sub>O (Hauri et al., 2015) and highly incompatible behavior of H<sub>2</sub>O during partial melting ( $D = 0.001$ ) yields 0.1–0.75 wt.% H<sub>2</sub>O in the melt. These amounts of water would increase the SCSS by an additional ~10 to 75 ppm.

#### 4.3. Evidence from sulfide-silicate partitioning of Ni, Co and Cu

Well-defined negative correlations exist between Ni and Co abundances and MgO contents in low- and high Ti lunar samples (e.g., Delano and Livi, 1981; Delano, 1986b; Ruzicka et al., 2001; Steenstra and van Westrenen, 2016; Fig. 9). For low-Ti basalts, it has been suggested that these relationships predominantly reflect olivine and/or possibly pyroxene fractionation processes (Walker et al., 1976a; Rhodes et al., 1977; Ringwood and Seifert, 1986; Delano, 1986b; Longhi, 1987; Papike et al., 1999; Ruzicka et al., 2001), as implied from experimental olivine-melt and pyroxene-melt partitioning data for Ni and Co (e.g., Irving, 1978; Green, 1994; Beattie, 1994; Jones, 1995; Papike et al., 1999; Matzen et al., 2017). Although unlikely from S systematics and abundances (Sections 4.1 and 4.2), fractional crystallization of sulfides would also result in depletions of Ni, Co and Cu due to their compatible behavior in sulfides (e.g., Kiseeva and Wood, 2015; this study). To test whether the Ni, Co and Cu abundances and systematics of low-Ti lunar basalts are compatible with fractional crystallization of (non)-stoichiometric sulfides, we use a Rayleigh-type crystal fractionation model to model the evolution of Ni, Co and Cu abundances in the absence and presence of sulfides (Eq. (16)):

$$\frac{C_L}{C_O} = F^{(D_i-1)} \quad (16)$$

where  $\frac{C_L}{C_O}$  is the ratio between the concentration of the element in the residual liquid ( $C_L$ ) and the element in the original magma ( $C_O$ ),  $F$  is the remaining melt fraction and  $D_i$  is the bulk distribution coefficient of trace element  $i$ . The  $D_i$  values were calculated using sulfide-silicate partition coefficients for Ni, Co and Cu that were obtained with expression of Kiseeva and Wood (2015), while assuming a FeO content of 20 wt.% and a stoichiometric FeS phase. In this approach it is assumed that the pressure effects on the sulfide-silicate partitioning behavior of Ni, Co and Cu are negligible, relative to effects of temperature (e.g., Li and Agee, 1996; Kiseeva and Wood, 2015), within the pressure range relevant for generation of low-Ti basalts (0.5–2.5 GPa; Table 6). The  $D_{Ni}^{olivine}$  values were modeled using the expression of Matzen et al. (2017). This expression includes a temperature dependency term as well as compositional terms that incorporate the effects of MgO in olivine and the silicate melt on Ni olivine-melt partitioning. For Co, we use the formulation of Jones (1995), where  $D_{Co}^{olivine}$  is calculated as a function of  $D_{Ni}^{olivine}$  (Jones, 1995; Papike et al., 1999). To our knowledge, no predictive model for  $D_{Cu}^{olivine}$  exists. We therefore assume  $D_{Cu}^{olivine} = 0.1$  for all modeled compositions and temperatures (Liu et al., 2014).

The liquid line of descent for low-Ti basalts at high pressure is not well constrained. We therefore assume that fractional crystallization starts at 1830 K for the most primitive low-Ti basalts and that it is reduced to 1430 K for the most evolved low-Ti basalts (Walker et al., 1976a). We consider 10% of fractional crystallization to have occurred across this compositional range, which is a reasonable estimate given the  $F$  factors inferred for low-Ti basalts (Table 6). The MgO contents of fractionating olivines were assumed to range between 43.5 and 30 wt.% for the most and least primitive basaltic compositions, respectively (Longhi et al., 1978). The corresponding modeled melt MgO contents ranged between 20 and 6.4 wt.%, corresponding with the range of the most and least primitive low-Ti basalts.

Fig. 9 shows the measured abundances of Ni, Co and Cu in various types of lunar low-Ti basalts as a function of basalt MgO content. As expected, Ni and Co behave compatible with increased fractionation of the magma – i.e. their concentrations in the low-Ti basalts decrease with decreasing MgO contents. For the Apollo 12 and 15 olivine basalts this decrease can be fully explained by the compatible behavior of Ni and Co in olivine during fractionation (Fig. 9a and b). This shows that the presence of sulfides is not required for explaining their abundances in the olivine basalts. The modeled Ni and Co contents for the pigeonite and ilmenite basalts are slightly higher, which may suggest that these melts experienced more than 10% olivine fractionation (Appendix Section A.3; Fig. S4).

Cu is similarly incompatible in both cpx and opx, whereas Ni and Co are compatible in opx and cpx, relative to olivine ( $D_{Ni}^{opx} = 1 - 7$ ;  $D_{Co}^{opx} = 1 - 2.5$ ;  $D_{Ni}^{cpx} = 2.8$ ;  $D_{Co}^{cpx} = 1$ ; e.g., Kennedy et al., 1993; Laubier et al., 2014; Liu et al., 2014). Fractionation of cpx and/or opx in addition to olivine will therefore not change these results significantly.

Although crystallization of minor amounts (<1.5%) of sulfides in addition to olivine would reproduce the slightly lower Ni contents measured in the pigeonite and ilmenite basalts, this cannot explain the much lower Co contents measured in the more evolved pigeonite and ilmenite basalts. It can also not be reconciled with the compatible behavior of chalcophile element Cu for these samples (Fig. 9c). It is therefore likely that the most evolved melts experienced slightly higher degrees of olivine fractionation than assumed here (Appendix Section A.3; Fig. S4).

Fractionation of non-stoichiometric sulfide compositions with 20 wt.% Ni results in an even higher expected depletion of Cu, whereas it does not significantly affect modeled Ni and Co abundances (Fig. S5). Addition of 20 wt.% Cu to the sulfide only slightly decreases the sulfide-silicate partition coefficients of Ni and Co, but additionally increases the chalcophile tendencies of Cu, relative to stoichiometric sulfides (Fig. S6). We therefore conclude that the presence of pure, Cu- or Ni-rich sulfide is not consistent with the observed Ni, Co and Cu systematics in low-Ti basalts. Finally, Cu abundances in low-Ti basalts could have been altered by degassing that occurred prior or during their eruption (Renggli et al., 2017). Degassing may explain some of the scatter observed for Cu within the A15 pigeonite basaltic suite (Fig. 9c). However, the overall incompatible behavior of Cu in low-Ti basalts that underwent variable degrees of fractional crystallization suggests that degassing is not the main process in controlling Cu abundances in low-Ti basalts.

#### 4.4. Implications of a S-poor lunar interior

Our results strongly suggest that the source regions of low-Ti basalts and volcanic glasses were not sulfide-saturated, unless > 90 per cent loss of S from all samples occurred during or after eruption. The more evolved (MgO-poor) A17 and/or A11 high-Ti basalts may have undergone sulfide saturation, but this has to be tested in future studies when high-pressure liquid lines of descent are available. Ding et al. (2017) recently came to a similar conclusion, but proposed that A11 high-Ti basalts may be sulfide-saturated if the sulfide is Ni-rich (> 30 wt.%). The presence of such Ni-rich sulfides seems to be excluded by the relatively low Ni contents measured in these magmas (Section 4.3). Our results suggest that the source regions of the primitive volcanic glasses and low-Ti basalts contained between 10 and 120 ppm S, which overlaps with the range as reported in Ding et al. (2017) for a smaller suite of lunar samples. It also overlaps with estimates of the S content of the bulk lunar interior ( $74.5 \pm 4.5$  ppm; Bombardieri et al., 2005; Chen et al., 2015; Hauri et al., 2015).

The inferred S-poor nature of the lunar interior adds strength to the hypothesis of a S-poor lunar core (<0.5 wt.% S; Righter et al., 2017a; Steenstra et al., 2017a) instead of a S-rich core (up to 12 wt.% S; e.g., Laneuville et al., 2014; Antonangeli et al., 2015). The hypothesis of the proposed similar S abundances in the bulk Moon and bulk silicate Earth when the siderophile behavior of S is taken into account also still holds (Steenstra et al., 2017a, 2017b). The

latter agrees with the relatively minor isotopic offset of S of the bulk Moon relative to the bulk silicate Earth (Wing and Farquhar, 2015). The absence of sulfides in the low-Ti basalt and volcanic glasses source regions also supports the hypothesis that the fractionated nature of highly siderophile element (HSE) patterns (e.g., Re/Os; Birck and Allegre, 1994) in these samples are the result of partial melting and mineral-melt fractionation processes, as suggested by Day et al. (2007) and Day and Walker (2015).

## 5. CONCLUSIONS

The sulfur concentration at sulfide saturation (SCSS) was determined for a range of low and high-Ti lunar melt compositions containing between 0.2 and 25 wt.% TiO<sub>2</sub>. It was found that the SCSS is strongly affected by the FeO, SiO<sub>2</sub> and Al<sub>2</sub>O<sub>3</sub> content of the silicate melt, resulting in SCSS values of up to 7400 ppm for the most Ti-rich Apollo 14 black glass. An increase in pressure reduces the SCSS value, whereas an increase in temperature increases the SCSS. A new empirical model that can be used to predict lunar SCSS values was developed, explicitly taking into account the composition of the sulfide melt. This model was calibrated from 1 atm–1423 K to up to 5 GPa - 2273 K and is suitable for predicting the SCSS for anhydrous, alkali-poor (K<sub>2</sub>O+Na<sub>2</sub>O < 5 wt.%) silicate melts with >5 wt.% to up to 40 wt.% FeO. It also accurately incorporates the effects of Ni and Cu in the sulfide on the SCSS at up to ~50 wt.% Cu and/or Ni.

Comparison between calculated SCSS values for low Ti basalts and low- and high-Ti volcanic glasses and the measured S abundances in these samples strongly suggest their source regions were not sulfide saturated. Extensive degassing of S from low-Ti basalts and all volcanic glasses are unlikely to have resulted in lowering the S abundances at SCSS to the S contents measured in these samples. In addition, our results show that segregation of (non)-stoichiometric sulfide phases would result in far more extensive depletions of Cu and to a lesser extent Ni and Co in lunar melts relative to observed values. A lack of sulfide saturation in their source regions agrees with previous studies that concluded Ni and Co systematics in these samples are predominantly set by olivine fractionation. As of yet we cannot exclude the possibility that perhaps the source regions of the most evolved high-Ti lunar basalts were sulfide saturated.

This work supports previous hypotheses of the S-poor nature of the lunar mantle and core. Our results show that sulfides have not affected the chalcophile and highly siderophile element systematics of low-Ti lunar basalts and volcanic glasses, and therefore, more likely represent a major phase of metal-silicate segregation (i.e. core formation).

## ACKNOWLEDGEMENTS

A.X.S., J.E., B.G.J.T. and F.P.F.W. performed experiments incorporated in this work as part of their undergraduate degree research projects. This work was supported financially by a Netherlands Organization for Scientific

Research (N.W.O.) Vici award to W.v.W. and by SFB TRR-170 (Publ. No. 33). We thank editor-in-chief M. Norman, associate editor M. Toplis and three anonymous reviewers for their critical and extensive reviews, that enabled us to improve our manuscript considerably.

## APPENDIX A. SUPPLEMENTARY MATERIAL

Supplementary data associated with this article can be found, in the online version, at <https://doi.org/10.1016/j.gca.2018.04.008>.

## REFERENCES

- Antonangeli D., Morard G., Schmerr N. C., Komabayashi T., Krisch M., Fiquet G. and Fei Y. (2015) Towards a mineral physics reference model for the Moon's core. *PNAS* **112**, 3916–3919.
- Arndt J. and von Engelhardt W. (1987) Formation of Apollo 17 orange and black glass beads. *Proc. 17th Lunar Planet. Sci. Conf. J. Geophys. Res.* **92**, E372–E376.
- Asimow P. D. and Longhi J. (2004) The significance of multiple saturation points in the context of polybaric near-fractional melting. *J. Petrol.* **45**, 2349–2367.
- Beard B. L., Taylor L. A., Scherer E. E., Johnson C. M. and Snyder G. A. (1998) The source region and melting mineralogy of high-titanium and low-titanium lunar basalts deduced from Lu-Hf isotope data. *Geochim. Cosmochim. Acta* **62**, 525–544.
- Beattie P. (1994) Systematics and energetics of trace-element partitioning between olivine and silicate melts: Implications for the nature of mineral/melt partitioning. *Chem. Geol.* **117**, 57–71.
- Birck J. L. and Allegre C. J. (1994) Contrasting Re/Os magmatic fractionation in planetary basalts. *Earth Planet. Sci. Lett.* **124**, 139–148.
- Bombardieri D. J., Norman M. D., Kamenetsky V. S. and Danyushevsky L. V. (2005) Major element and primary sulfur concentrations in Apollo 12 mare basalts: The view from melt inclusions. *Meteorit. Planet. Sci.* **40**, 679–693.
- Boujibar A., Andraut D., Bouhifd M. A., Bolfan-Casanova N., Devidal J. L. and Trcera N. (2014) Metal-silicate partitioning of sulphur, new experimental and thermodynamic constraints on planetary accretion. *Earth Planet. Sci. Lett.* **391**, 42–54.
- Boyd F. R. and England J. L. (1960) Apparatus for phase-equilibrium measurements at pressures up to 50 kilobars and temperatures up to 1750 °C. *J. Geophys. Res.* **65**, 741–748.
- Brenan J. M. (2008) Re-Os fractionation by sulfide melt-silicate melt partitioning: A new spin. *Chem. Geol.* **248**, 140–165.
- Brett R. (1976) Reduction of mare basalts by sulfur loss. *Lunar Planet. Sci. Conf.* **6**, 89.
- Capobianco C. J., Drake M. J. and De'Aro J. (1999) Siderophile geochemistry of Ga, Ge, and Sn: Cationic oxidation states in silicate melts and the effect of composition in iron-nickel alloys. *Geochim. Cosmochim. Acta* **63**, 2667–2677.
- Chen Y., Zhang Y., Liu Y., Guan Y., Eiler J. and Stolper E. M. (2015) Water, fluorine, and sulfur concentrations in the lunar mantle. *Earth Planet. Sci. Lett.* **427**, 37–46.
- Corgne A., Keshav S., Wood B. J., McDonough W. F. and Fei Y. (2008) Metal-silicate partitioning and constraints on core composition and oxygen fugacity during Earth accretion. *Geochim. Cosmochim. Acta* **72**, 574–589.
- Danckwerth, P.A., Hess, P.C., Rutherford, M.J., 1979. The solubility of sulfur in high-TiO<sub>2</sub> mare basalts. *Lunar Planet. Sci. Conf.* 10th, 517–530.
- Day J. M. D., Pearson D. G. and Taylor L. A. (2007) Highly siderophile element constraints on accretion and differentiation of the Earth-Moon system. *Science* **315**, 217–219.
- Day J. M. D. and Walker R. J. (2015) Highly siderophile element depletion in the Moon. *Earth Planet. Sci. Lett.* **423**, 114–124.
- Delano J. W. (1980) Chemistry and liquidus phase relations of Apollo 15 red glass Implications for the deep lunar interior. *Lunar Planet. Sci. Conf.* **1**, 251–288.
- Delano J. W. (1986a) Pristine lunar glasses: Criteria, Data and implications. *Proc. 16th Lunar Planet. Sci. Conf. J. Geophys. Res.* **91**, D201–D213.
- Delano, J.W., 1986. Abundances of cobalt, nickel, and volatiles in the silicate portion of the Moon. In: *Origin of the Moon*.
- Delano J. W. and Livi K. (1981) Lunar volcanic glasses and their constraints on mare petrogenesis. *Geochim. Cosmochim. Acta* **45**, 2137–2149.
- Delano, J.W., Hanson, B.Z., Watson, W.B., 1994. Abundance and Diffusivity of Sulfur in Lunar Picritic Magmas. *Lunar Planet. Sci. Conf.* 25th, 325.
- Ding S., Dasgupta R. and Tsuno K. (2014) Sulfur concentration of martian basalts at sulfide saturation at high pressures and temperatures - Implications for deep sulfur cycle on Mars. *Geochim. Cosmochim. Acta* **131**, 227–246.
- Ding S., Hough T. and Dasgupta R. (2017) New high pressure experiments on sulfide saturation of high-FeO\* basalts with variable TiO<sub>2</sub> contents - Implications for the sulfur inventory of the lunar interior. *Geochim. Cosmochim. Acta* **222**, 319–339.
- Elkins L. T., Fernandes V. A., Delano J. W. and Grove T. L. (2000) Origin of lunar ultramafic green glasses: Constraints from phase equilibrium studies. *Geochim. Cosmochim. Acta* **64**, 2339–2350.
- Elkins-Tanton L. T., Chatterjee N. and Grove T. L. (2003) Experimental and petrological constraints on lunar differentiation from the Apollo 15 green picritic glasses. *Meteorit. Planet. Sci.* **38**, 515–527.
- Farquhar J., Bao H. and Thiemens M. (2000) Atmospheric influence of earth's earliest sulfur cycle. *Science* **289**, 756–758.
- Fincham C. J. B. and Richardson F. D. (1954) The behaviour of sulphur in silicate and aluminate melts. *Proc. R. Soc. A Math. Phys. Eng. Sci.* **223**, 40–62.
- Fortin M.-A., Riddle J., Desjardins-Langlais Y. and Baker D. R. (2015) The effect of water on the sulfur concentration at sulfide saturation (SCSS) in natural melts. *Geochim. Cosmochim. Acta* **160**, 100–116.
- Gibson, E.K., Chang, S., Lennon, K., More, G.W., Pearce, G.W., 1975. Sulfur abundances and distributions in mare basalts and their source magmas. *Proc. Lunar Sci. Conf.* 6th, 1287–1301.
- Gibson, E.K., Usselman, T.M., Morris, R.V., 1976. Sulfur in the Apollo 17 basalts and their source regions. *Proc. Lunar Sci. Conf.* 7th, 1491–1505.
- Green, D.H., Ringwood, A.E., Hibberson, W.O., Ware, N.G., 1975. Experimental petrology of Apollo 17 mare basalts. *Lunar Planet. Sci. Conf.* 6th, 871–893.
- Green T. H. (1994) Experimental studies of trace-element partitioning applicable to igneous petrogenesis-Sedona 16 years later. *Chem. Geol.* **117**, 1–36.
- Gudmundsson G. and Holloway J. R. (1993) Activity-composition relationships in the system Fe-Pt at 1300 and 1400C and at 1 atm and 20 kbar. *Am. Mineral.* **78**, 178–186.
- Hauri E. H., Weinreich T., Saal A. E., Rutherford M. C. and van Orman J. A. (2011) High pre-eruptive water contents preserved in lunar melt inclusions. *Science* **333**, 213–215.
- Hauri E. H., Saal A. E., Rutherford M. J. and van Orman J. A. (2015) Water in the Moon's interior: Truth and consequences. *Earth Planet. Sci. Lett.* **409**, 252–264.

- Holzheid A. and Grove T. L. (2002) Sulfur saturation limits in silicate melts and their implications for core formation scenarios for terrestrial planets. *Am. Mineral.* **87**, 227–237.
- Hughes S. S., Delano J. W. and Schmitt R. A. (1988) Apollo 15 yellow-brown volcanic glass: Chemistry and petrogenetic relations to green volcanic glass and olivine-normative mare basalts. *Geochim. Cosmochim. Acta* **52**, 2379–2391.
- Hughes, S.S., Delano, J.W., Schmitt, R.A., 1989. Petrogenetic modeling of 74220 high-Ti orange volcanic glasses and the Apollo 11 and 17 high-Ti mare basalts. Proc. Lunar Sci. Conf. 19th, 175–188.
- Irving A. J. (1978) A review of experimental studies of crystal/liquid trace element partitioning. *Geochim. Cosmochim. Acta* **42**, 743–770.
- Jugo P., Luth R. W. and Richards J. P. (2005) An experimental study of the sulfur content in basaltic melts saturated with immiscible sulfide of sulfate liquids at 1300 degrees celcius and 1 GPa. *J. Petrol.* **46**(4), 783–798.
- Jones J. H. (1995) Experimental trace element partitioning. In: Rock physics and phase relations, a handbook of physical constants, A.G.U. reference shelf 3. AGU, 73–104.
- Kato C. and Moynier F. (2017) Gallium isotopic evidence for extensive volatile loss from the Moon during its formation. *Sci. Adv.* **3**, e1700571.
- Kennedy A. K., Lofgren G. E. and Wasserburg G. J. (1993) An experimental study of trace element partitioning between olivine, orthopyroxene and melt in chondrules: equilibrium values and kinetic effects. *Earth Planet. Sci. Lett.* **115**, 177–195.
- Kessel R., Beckett J. R. and Stolper E. M. (2001) Thermodynamic properties of the Pt-Fe system. *Am. Mineral.* **86**, 1003–1014.
- Kiseeva E. S. and Wood B. J. (2013) A simple model for chalcophile element partitioning between sulphide and silicate liquids with geochemical applications. *Earth Planet. Sci. Lett.* **383**, 68–81.
- Kiseeva E. S. and Wood B. J. (2015) The effects of composition and temperature on chalcophile and lithophile element partitioning into magmatic sulphides. *Earth Planet. Sci. Lett.* **424**, 280–294.
- Krawczynski, M.J., Grove, T.L., 2008. Experimental investigation of fO<sub>2</sub> effects on Apollo 17 orange glass phase equilibria. Lunar Planet. Sci. Conf. 39, #1231 (abstr.).
- Laneuville M., Wieczorek M. A., Breuer D., Aubert J., Morard G. and Ruckriemen T. (2014) A long-lived lunar dynamo powered by core crystallization. *Earth Planet. Sci. Lett.* **401**, 251–260.
- Laubier M., Grove T. L. and Langmuir C. H. (2014) Trace element mineral/melt partitioning for basaltic and basaltic andesitic melts: An experimental and laser ICP-MS study with application to the oxidation state of mantle source regions. *Earth Planet. Sci. Lett.* **392**, 265–278.
- Laurenz V., Rubie D. C., Frost D. J. and Vogel A. K. (2016) The importance of sulfur for the behavior of highly-siderophile elements during Earth's differentiation. *Geochim. Cosmochim. Acta* **194**, 123–138.
- Lee J. H. and Morita K. (2002) Evaluation of surface tension and adsorption for liquid Fe-S alloys. *ISIJ Int.* **42**, 588–594.
- Li J. and Agee C. B. (1996) Geochemistry of mantle-core differentiation at high pressure. *Nature* **381**, 686–689.
- Li J. and Agee C. B. (2001) Element partitioning constraints on the light element composition of the Earth's core. *Geophys. Res. Lett.* **28**, 81–84.
- Lin Y. H., Tronche E. J., Steenstra E. S. and van Westrenen W. (2017) Evidence for an early wet Moon from experimental crystallization of the lunar magma ocean. *Nat. Geosci.* **10**, 14–18.
- Liu Y., Samaha N.-T. and Baker D. R. (2007) Sulfur concentration at sulfide saturation (SCSS) in magmatic silicate melts. *Geochim. Cosmochim. Acta* **71**, 1783–1799.
- Liu X., Xiong X., Audetat A., Li Y., Song M., Li L., Sun W. and Ding X. (2014) Partitioning of copper between olivine, orthopyroxene, clinopyroxene, spinel, garnet and silicate melts at upper mantle conditions. *Geochim. Cosmochim. Acta* **125**, 1–22.
- Longhi, J., Walker, D., Grove, T.L., Stolper, E.M., Hays, J.F., 1974. The petrology of the Apollo 17 mare basalts. In: Proc. 5th Lunar Conf., pp. 447–469.
- Longhi J., Walker D. and Hays J. F. (1978) The distribution of Fe and Mg between olivine and lunar basaltic liquids. *Geochim. Cosmochim. Acta* **42**, 1545–1558.
- Longhi J. (1987) On the connection between mare basalts and picritic volcanix glasses. *Proc. 17th Lunar Planet. Sci. Conf. JGR* **92**, E349–E360.
- Marvin U. B. and Walker D. (1978) Implications of a titanium-rich glass clod at Oceanic Procellarum. *Am. Mineral.* **63**, 924–929.
- Matzen A. K., Baker M. B., Beckett J. R., Wood B. J. and Stolper E. M. (2017) The effect of liquid composition on the partitioning of Ni between olivine and silicate melt. *Contrib. Mineral. Petrol.* **172**(1), 3.
- Mavrogenes J. A. and O'Neill H. S. C. (1999) The relative effects of pressure, temperature and oxygen fugacity on the solubility of sulfide in mafic magmas. *Geochim. Cosmochim. Acta* **63**, 1173–1180.
- Médard E., McCammon C. A., Barr J. A. and Grove T. L. (2008) Oxygen fugacity, temperature reproducibility, and H<sub>2</sub>O contents of nominally anhydrous piston-cylinder experiments using graphite capsules. *Am. Mineral.* **93**, 1838–1844.
- Meyer, C., 2011. The lunar sample compendium. <http://curator.jsc.nasa.gov/Lunar/lsc/index/cfm>. Accessed 25 April 2017.
- Mungall J. E. and Brenan J. M. (2014) Partitioning of platinum-group elements and Au between sulphide liquid and basalt and the origins of mantle-crust fractionation of the chalcophile elements. *Geochim. Cosmochim. Acta* **125**, 265–269.
- Nagamori M. and Yazawa A. (2001) Thermodynamic observations of the molten FeS-FeO system and its vicinity at 1473 K. *Metall. Mater. Trans. B Process Metall. Mater. Process. Sci.* **32**, 831–837.
- Neal C. R., Taylor L. A., Hughes S. S. and Schmitt R. A. (1990) The significance of fractional crystallization in the petrogenesis of Apollo 17 Type A and B high-Ti basalts. *Geochim. Cosmochim. Acta* **54**, 1817–1833.
- Neal C. R. and Taylor L. A. (1992) Petrogenesis of mare basalts: A record of lunar volcanism. *Geochim. Cosmochim. Acta* **56**, 2177–2211.
- O'Neil H. S. T. C. and Mavrogenes J. A. (2002) The sulfide capacity and the sulfur content at sulfide saturation of silicate melts at 1400 C and 1 bar. *J. Petrol.* **43**, 1049–1087.
- Paniello R. C., Day J. M. D. and Moynier F. (2012) Zinc isotopic evidence for the origin of the Moon. *Nature* **490**, 376–379.
- Papike J. J., Hodges F. N., Bence A. E., Cameron M. and Rhodes J. M. (1976) Mare basalts: Crystal chemistry, mineralogy, and petrology. *Rev. Geophys.* **14**, 475–540.
- Papike J. J., Fowler G. W., Adcock C. T. and Shearer C. K. (1999) Systematics of Ni and Co in olivine from planetary melt systems: Lunar mare basalts. *Am. Mineral.* **84**, 392–399.
- Renggli C. J., King P. L., Henley R. W. and Norman M. D. (2017) Volcanic gas composition, metal dispersion and deposition during explosive volcanic eruptions on the Moon. *Geochim. Cosmochim. Acta* **206**, 296–311.
- Rhodes J. M., Brannon J. C., Rodgers K. V., Blancard D. P. and Dungan M. A. (1977) Chemistry of Apollo 12 mare basalts – Magma types and fractionation processes. 8th Lunar Sci. Conf., pp. 1305–1338.

- Righter K., Pando K. and Danielson L. R. (2009) Experimental evidence for sulfur-rich martian magmas: Implications for volcanism and surficial sulfur sources. *Earth Planet. Sci. Lett.* **288**, 235–243.
- Righter K., Danielson L. R., Pando K. M., Shofner G. A., Sutton S. R., Newville M. and Lee C. T. (2016) Valence and metal/silicate partitioning of Mo: Implications for conditions of Earth accretion and core formation. *Earth Planet. Sci. Lett.* **437**, 89–100.
- Righter K., Go B. M., Pando K. A., Danielson L., Ross D. K., Zahman Z. and Keller L. P. (2017a) Phase equilibria of a low S and C lunar core: Implications for an early lunar dynamo and physical state of the current core. *Earth Planet. Sci. Lett.* **463**, 323–332.
- Righter K., Nickodem K., Pando K., Danielson L., Boujibar A., Righter M. and Lapen T. J. (2017b) Distribution of Sb, As, Ge, and In between metal and silicate during accretion and core formation in the Earth. *Geochim. Cosmochim. Acta* **198**, 1–16.
- Ringwood A. E. and Seifert S. (1986) Nickel-cobalt abundance systematics and their bearing on lunar origin. In: *Origin of the Moon*.
- Ruzicka A., Snyder G. A. and Taylor L. A. (2001) Comparative geochemistry of basalts from the Moon, Earth, HED asteroid, and Mars: Implications for the origin of the Moon. *Geochim. Cosmochim. Acta* **65**, 979–997.
- Rutherford M. J., Hess P. C. and Daniel G. H. (1974) Experimental liquid line of descent and liquid immiscibility for basalt 70017. *Lunar Planet. Sci. Conf. 5th*, pp. 569–583.
- Saal A. E., Hauri E. H., Cascio M. L., van Orman J. A., Rutherford M. C. and Cooper R. F. (2008) Volatile content of lunar volcanic glasses and the presence of water in the Moon's interior. *Nature* **454**, 192–195.
- Sarafian E., Gaetani G. A., Hauri E. H. and Sarafian A. R. (2017) Experimental constraints on the damp peridotite solidus and oceanic mantle potential temperature. *Science* **355**, 942–945.
- Shearer C. K., Papike J. J., Galbreath K. C. and Shimizu N. (1991) Exploring the lunar mantle with secondary ion mass spectrometry: a comparison of lunar picritic glass beads from the Apollo 14 and Apollo 17 sites. *Earth Planet. Sci. Lett.* **102**, 134–147.
- Shearer C. K., Papike J. J. and Layne G. D. (1996) The role of ilmenite in the source region for mare basalts: Evidence from niobium, zirconium, and cerium in picritic glasses. *Geochim. Cosmochim. Acta* **60**, 3521–3530.
- Siebert J., Corgne A. and Ryerson F. J. (2011) Systematics of metal-silicate partitioning for many siderophile elements applied to Earth's core formation. *Geochim. Cosmochim. Acta* **75**, 1451–1489.
- Smythe D. J., Wood B. J. and Kiseeva E. S. (2017) The S content of silicate melts at sulfide saturation: New experiments and a model incorporating the effects of sulfide composition. *Am. Mineral.* **102**, 795–803.
- Snyder G. A., Taylor L. A. and Neal C. R. (1992) A chemical model for generating the sources of mare basalts: Combined equilibrium and fractional crystallization of the lunar magmasphere. *Geochim. Cosmochim. Acta* **56**, 3809–3823.
- Steenstra E. S. and van Westrenen W. (2016) Siderophile elements in the lunar mantle. Chapter in: *Encyclopedia of Lunar Science* (doi: 10.1007/978-3-319-05546-6\_76-1).
- Steenstra E. S., Rai N., Knibbe J. S., Lin Y. H. and van Westrenen W. (2016) New geochemical models of core formation in the Moon from metal-silicate partitioning of 15 siderophile elements. *Earth Planet. Sci. Lett.* **441**, 1–9.
- Steenstra E. S., Lin Y. H., Rai N., Jansen M. and van Westrenen W. (2017a) Carbon as the dominant light element in the lunar core. *Am. Mineral.* **102**, 92–97.
- Steenstra E. S., Lin Y., Dankers D., Rai N., Berndt J., Matveev S. and van Westrenen W. (2017b) The lunar core can be a major reservoir for volatile elements S, Se, Te and Sb. *Sci. Rep.* **7**, 14552.
- Steenstra E. S., Sitabi A. B., Lin Y. H., Rai N., Knibbe J. S., Berndt J., Matveev S. and van Westrenen W. (2017c) The effect of melt composition on metal-silicate partitioning of siderophile elements and constraints on core formation in the angrite parent body. *Geochim. Cosmochim. Acta* **212**, 62–83.
- Tartèse R., Anand M., Barnes J. J., Starkey N. A., Franchi I. A. and Sano Y. (2013) The abundance, distribution, and isotopic composition of Hydrogen in the Moon as revealed by basaltic lunar samples: Implications for the volatile inventory of the Moon. *Geochim. Cosmochim. Acta* **122**, 58–74.
- Vander Kaaden K. E., Agee C. B. and McCubbin F. M. (2015) Density and compressibility of the molten lunar picritic glasses: Implications for the roles of Ti and Fe in the structures of silicate melts. *Geochim. Cosmochim. Acta* **149**, 1–20.
- Van Kan Parker M., Agee C. B., Duncan M. S. and van Westrenen W. (2011a) Compressibility of molten Apollo 17 orange glass and implications for density crossovers in the lunar mantle. *Geochim. Cosmochim. Acta* **75**, 1161–1172.
- Van Kan Parker M., Mason P. R. D. and van Westrenen W. (2011b) Experimental study of trace element partitioning between lunar orthopyroxene and anhydrous silicate melt: Effects of lithium and iron. *Chem. Geol.* **285**, 1–14.
- Wagner T. P. and Grove T. L. (1997) Experimental constraints on the origin of lunar high-Ti ultramafic glasses. *Geochim. Cosmochim. Acta* **61**, 1315–1327.
- Walker D., Longhi J., Kirkpatrick R. J. and Hays J. F. (1976a) Differentiation of an Apollo 12 picrite magma. *7th Proc. Lunar Sci. Conf.*, pp. 1365–1389.
- Walker D., Kirkpatrick R. J., Longhi J. and Hays J. F. (1976) Crystallization history of lunar picritic basalt sample 12002: Phase-equilibria and cooling-rate studies. *GSA Bull.* **87**(5), 646–656.
- Wang Z. and Becker H. (2013) Ratios of S, Se and Te in the silicate Earth require a volatile-rich late veneer. *Nature* **499**, 328–331.
- Wang Z., Laurenz V., Petitgirard S. and Becker H. (2016) Earth's moderately volatile element composition may not be chondritic: Evidence from In, Cd and Zn. *Earth Planet. Sci. Lett.* **435**, 136–146.
- Wendlandt R. F. (1982) Sulfide saturation of basalt and andesite melts at high pressure and temperatures. *Am. Mineral.* **67**, 877–885.
- Wing B. A. and Farquhar J. (2015) Sulfur isotope homogeneity of lunar mare basalts. *Geochim. Cosmochim. Acta* **170**, 266–280.
- Wohlert A. and Wood B. J. (2015) A Mercury-like component of early Earth yields uranium in the core and high mantle <sup>142</sup>Nd. *Nature* **520**, 337–340.
- Wood B. J. and Kiseeva E. S. (2015) Trace element partitioning into sulfide: How lithophile elements become chalcophile and vice versa. *Am. Mineral.* **100**, 2371–2379.
- Wood B. J., Kiseeva E. S. and Mirolo F. J. (2014) Accretion and core formation: the effects of sulfur on metal-silicate partition coefficients. *Geochim. Cosmochim. Acta* **145**, 248–267.
- Wykes J. L., O'Neill H. St. C. and Mavrogenes J. A. (2015) The effect of FeO on the sulfur content at sulfide saturation (SCSS) and the selenium content at selenide saturation of silicate melts. *J. Petrol.* **56**, 1407–1424.
- Zhang Y., Ni H. and Chen Y. (2010) Diffusion data in silicate melts. *Rev. Mineral. Geochem.* **72**, 311–408.